

**Effect of Valency on the Dynamics and
Thermodynamics of DNA-linked Nanoparticles
Materials**

by

Wei Dai 戴維

Class of 2011

A thesis submitted to the
faculty of Wesleyan University
in partial fulfillment of the requirements for the
Degree of Bachelor of Arts
with Departmental Honors in Physics

*To my two grandmothers,
who had not learned physics, but nonetheless
left indelible memories in a young physicist's heart
when they were still with us.*

Abstract

Nanoparticles (NP) functionalized with single-stranded DNA (ssDNA) offer a route to custom-designed, self-assembled nanomaterials with potentially unusual properties. We explore the phase behavior and structure of a model for NP functionalized with between 3 and 6 short ssDNA through simulations, allowing us to examine both the role of the number of attached strands (valency) and their relative orientations. We find that 3 to 5-functionalized NP form amorphous systems, with 4 and 5-functionalized NP constructing an unusual multitude of liquid phases, or polyamorphism, through interpenetration of networks. The 6-functionalized NP with octahedral symmetry form at least six crystalline structures, consisting of up to six interpenetrating simple cubic lattices. The crystallization dynamics of the 6-functionalized system follows the conventional two-step pathway, demonstrating that such mechanism applies to our NP system with complex interactions.

Acknowledgments

I want to first thank my advisor Francis W. Starr, who stands as a star personage in my research discoveries and my personal growth at Wesleyan. I also want to thank my labmates, who have added much laughter to my time in the lab during the past three years. And I am more than excited to express my appreciation to all professors in the department for your thought-provoking lectures and next-to-impossible problem sets. From your teaching I am convinced that physics is indeed hard and interesting.

I am deeply grateful for the generosity of the Freeman Asian Scholarship Program, because of which I could pursue physics at Wesleyan. I also owe much to my beloved families, who continuously support me on my path of science. *Thank you.*

Finally, I want to give special thanks to the Creator God, who has so meticulously and wonderfully designed the nano-world which I am now going to talk about.

Contents

1	Introduction	1
1.1	DNA as a Guide to Self-assembled Nanomaterials	3
1.2	Experimental Developments	5
1.3	Phase Behaviors of DNA-Functionalized Nanoparticles	8
1.4	Theory of Crystallization Process	11
1.5	Study Objectives and Result Summaries	12
1.6	Organizations of the Thesis	14
2	Model and Simulation Methods	16
2.1	Coarse-Grained Model	16
2.2	Effective Potential Model	19
2.3	Studied Variations of Geometry	22
2.4	Simulation Methods	24
3	Amorphous Systems	26
3.1	Phase Behaviors	26
3.1.1	Valency Dependence of Phase Boundaries	31
3.2	Structure	34
3.2.1	Pair Correlation Function	34
3.2.2	Chemical Distance Analysis	35

4 Crystal Systems	39
4.1 Phase Behaviors	39
4.2 Structure	45
4.3 Crystallization Dynamics	48
4.3.1 Cluster Size and Global Order Parameters	49
4.3.2 Identification of Crystalline Clusters	52
4.3.3 Time Evolution of Crystallization	55
5 Discussion	60
5.1 Interpenetration of Networks and Lattices	60
5.2 Crystallization Process	64
5.2.1 Comparison with Experiments	65
5.2.2 Why is Crystallization Hard?	67
6 Conclusion	70

List of Figures

1.1	A schematic of self-assembly	2
1.2	“Quantum corral” created by scanning tunneling microscope (STM).	2
1.3	Self-assembly through DNA strand hybridization.	4
1.4	A snapshot of the network formed by the DNA-functionalized nanoparticles from computer simulation.	5
1.5	A schematic of a ssDNA bond mediated by linker DNA.	6
1.6	Micrometer-sized colloids grafted with oligonucleotides and the formed amorphous aggregates	6
1.7	DNA-linked gold nanoparticles.	7
1.8	A cartoon visualization of a single network created by NP functionalized with 4 ssDNA.	9
1.9	A cartoon visualization of two and three interpenetrating networks created by NP functionalized with 4 ssDNA.	10
2.1	Schematic of the coarse-grained model of DNA.	17
2.2	Lennard-Jones (LJ) and FENE potential.	18
2.3	Schematic of parametrization of the coarse-grained model.	20
2.4	Cartoon of the geometries of the DNA functionalized nanoparticles studied	23
3.1	The $T - \rho$ phase diagram for four amorphous systems.	27
3.2	Scaled $T - \rho$ phase diagram for amorphous systems.	30

3.3	Schematic representation of the location of the “sticky patches” in a previously studied model.	31
3.4	Gas-liquid coexistence curves of a previously studied model with limited valency.	32
3.5	The radial distribution function $g(r)$ for networked amorphous states.	33
3.6	$g(r)$ restricted to bonded neighbors up to a chemical distance D	36
3.7	Visualization of two interpenetrating networks for 5-SBP system at local scope.	37
4.1	$\rho - \mu$ phase diagram of 6 crystals at $T = 0.08311$	40
4.2	Visualization of the interpenetrating lattices of crystal I–VI.	42
4.3	The percentage of intact bonds as a function of T on heating for crystal I–V.	43
4.4	$T - \rho$ phase diagram of multiple crystals formed by octahedral nanoparticles.	44
4.5	Bond energy per particle as a function of crystal hierarchy (crystal I–VI).	46
4.6	$S(q)$ for the hierachial crystal phases formed by octahedral geometry.	47
4.7	The close-up of the phase diagram at crystal I and II	50
4.8	The distribution of the values of $\mathbf{q}_4(\mathbf{i}) \cdot \mathbf{q}_4(\mathbf{j})$ for amorphous and crystal systems.	53
4.9	The distribution of the number of neighbors with “crystal-like connection” for amorphous and crystal systems.	54
4.10	The time evolution of clustering and crystallization process of three investigated systems.	56
4.11	The crystallization time τ for the 6-functional NP system at $\rho d^3 = 0.5$	57
4.12	Visualization of the crystal lattices prior, during, and after nucleation for systems at $\rho d^3 = 0.5$ and $\rho d^3 = 1.5$	59
5.1	Gas-liquid phase transition boundary in $T - \rho$ plane.	62
5.2	The model and phase diagram of the 6-functional patchy particles.	63

5.3	Double strand DNA helix.	63
5.4	The schematic of the three-step crystallization pathway.	66
5.5	The possibility of DNA-functionalized NP bonding via isotropic attractive core-core interaction.	67
5.6	The schematic of the free energy pathway of crystallization.	68

Chapter 1

Introduction

Nanotechnology is the study of systems at the atomic or molecular levels, typically at length scales from 1 to 100 nanometer. At this scale, it is possible to control the molecular details and their integration into larger architectures, which is the so-called “bottom-up” approach to nanotechnological construction. In this approach, artificially designed molecules self-assemble in parallel steps following their pre-programmed molecular recognition properties (Fig. 1.1). In contrast, the “top-down” approach of nanofabrication achieves the control of molecular details, such as precisely patterning atoms on a surface (Fig. 1.2 [1]), by using microscopy tips or through photolithography process. Compared with the top-down approach, the bottom-up method through route of self-assembly can potentially create large structures more efficiently and at lower costs [2]. Due to these advantages, self-assembly is currently a focused subject of research in nanotechnology [3–5].

In this direction, the main objective is to devise molecules that can serve as “building blocks” which self-assemble into desired structures through controlled routes. A wide range of experiments have fabricated building blocks comprised of atoms, molecules, macromolecules or colloidal particles [7, 8]. Recently, scientists found that the application of biological construction to artificially devised complexes holds great promise

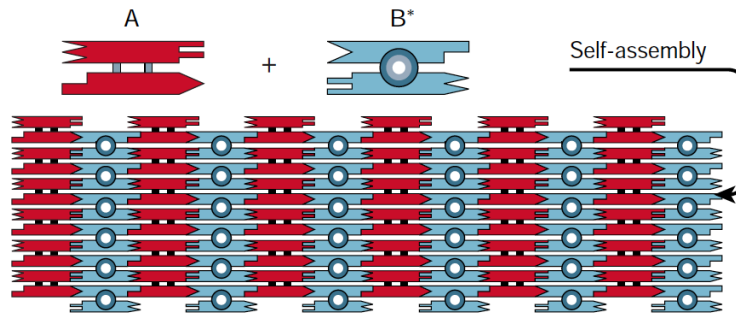


Figure 1.1: A schematic of self-assembly in ref. [6]. The nano-building blocks self-organize through parallel steps following the pre-designed molecular features.

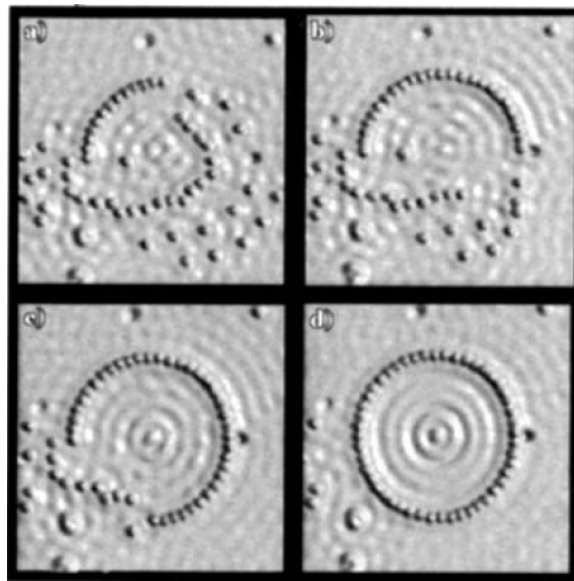


Figure 1.2: “Quantum corral” created by scanning tunneling microscope (STM) in ref. [1]. At 4°K in ultrahigh vacuum, Eigler and co-workers used STM to arrange 48 Fe atoms into a ring of diameter 14.3 nm on a Cu(111) surface, which can then be used to study the electrons trapped in two dimensional state. (a)–(c) are snapshots during the production, and (d) is the finished structure. The fringes in (d) are caused by wave scatters.

for the development of self-assembled nanostructures and materials [4, 9–11]. Among the many choices, DNA has features that are particularly attractive for use in nanotechnology. There has been a wide range of experimentally synthesized DNA-modified nanoparticles [6, 12], along with theoretical descriptions of this new class of material [13–19]. In this thesis, we take advantage of the control offered by computer simulations to investigate the self-assembly structures and dynamics of DNA-functionalized nanoparticles.

1.1 DNA as a Guide to Self-assembled Nanomaterials

DNA is a nucleic acid formed by sequence of nucleotide bases adenine (A), thymine (T), cytosine (C), and guanine (G). The size of DNA falls in the nano-scale: a ssDNA has a diameter about 2 nm, and each nucleotide unit is 0.33 nm long. In addition, DNA retains some “stiffness”; the persistence length of duplex DNA amounts to ≈ 50 nm. This size and stiffness is ideal for DNA to be the nano-scaled linker of self-assmbling building blocks.

The real advantage of DNA lies in the control of DNA binding, which is a consequence of two properties: bonding specificity and “lock-and-key” interactions. The bonding specificity arises from the nucleotide base pair recognition properties. Specifically, when two single-stranded DNA (ssDNA) “zip” to form a double-stranded DNA (dsDNA), the nucleotide bases adenine (A) only bonds to thymine (T), and cytosine (C) only bonds to guanine (G). The binding results in a double helix of DNA consisted of two negatively charged phosphate-sugar polymer chains held together by hydrogen bonds between complementary bases on each chain. By controling the base sequence of a ssDNA, one can design the bonding (complementary base sequence) or non-bonding (non-complementary base sequence) interaction between two ssDNA. Furthermore, the bonding between two nucleotide bases excludes the the possibility of binding to a third nucleotide base, so that the binding of two ssDNA prevents the binding to the third ssDNA. This desired

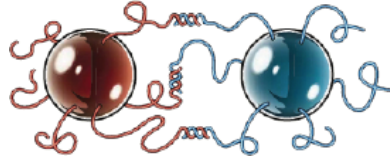


Figure 1.3: NP functionalized with multiple ssDNA strands that forms dsDNA to bond with the other NP. Picture from ref. [12].

“lock-and-key” interaction gives better control of the number of bonded NP as each ssDNA “arm” can join only one other NP. Additionally, the dsDNA bond is reversible through denaturation, allowing local rearrangement of undesired bonds and change of global structure by controlling the thermal conditions. Together, the lock-and-key interactions, bonding specificity, and bond reversibility offer a route to design highly organized materials through the synthetic bottom-up approach.

The drawback of DNA is that topologically it is one dimensional, and linking DNA will only create long chains. In order to form complex DNA-based networks, it is necessary for linear ssDNA or double stands (dsDNA) to be linked by junctions, either formed by a branched DNA structure [20–22] such as Holiday junction or by tethering the DNA to a vertex unit [9, 23]. Here we consider the second approach: by grafting multiple ssDNA to a NP and an intelligent choice for the base sequence, one can potentially create complex structures, because ssDNA attached to different NPs can hybridize into dsDNA, physically linking the particles (Fig. 1.3). The NP thus act as nodes of the DNA-linked network [23]. An example is visualized to demonstrate this point (Figure 1.4). Therefore, it is possible to control the local geometry of the networks by specifying the number and orientation of the attached ssDNA to the NP, which in turn may control the geometry of higher-order structures [24]. This approach to construct macroscopic materials from bottom-up self-assembling construction can potentially result in a precision hard to achieve by molecular nano-fabrication, with promising future applications in optical and electrical materials [6, 12, 25].

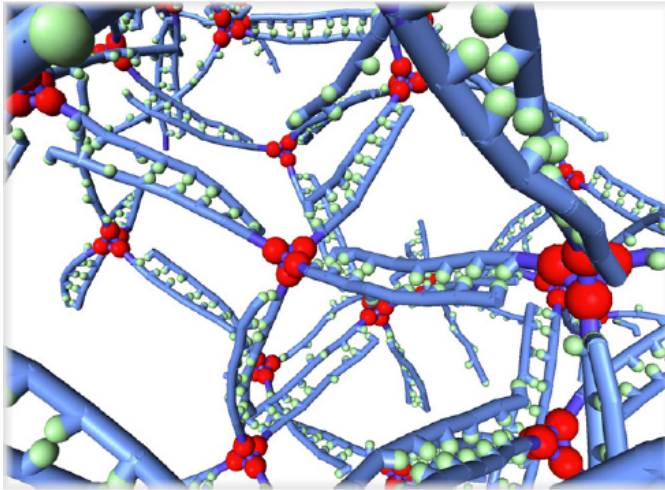


Figure 1.4: A snapshot of the network formed by the DNA-functionalized nanoparticles from computer simulation in ref [17]. The constituent units are nanoparticles (the red hub) functionalized with four 8-base ssDNA (the blue tube with green spheres representing base sequence) in tetrahedral coordination.

1.2 Experimental Developments

Most experimental studies create NP functionalized with non-complementary ssDNA. The binding of NP is achieved by introducing the “linker” DNA with sequence whose ends can bind to ssDNA of NP, thus enabling the connection between two ssDNA [26–28]. It is also common to use double-stranded DNA (dsDNA) in the “spacer region” to enhance the stiffness of the tether DNA, although the bonding still occurs at the ssDNA end via linker DNA via linker DNA (Fig. 1.5) [29]. There is also another design that allows the ssDNA end to directly bond to the ssDNA from the other NP, which does not require linker DNA [30–33].

In terms of functionalization, most studies of DNA functionalized particles have explored uniform coverage of micron size colloids [26–28, 32, 33] or nanoscale gold NP [34, 35]. One example is the reversible self-assembly micrometer-sized colloid mediated by oligonucleotides, or short nucleic acid polymers (Fig. 1.6) [26]. Smaller size NP

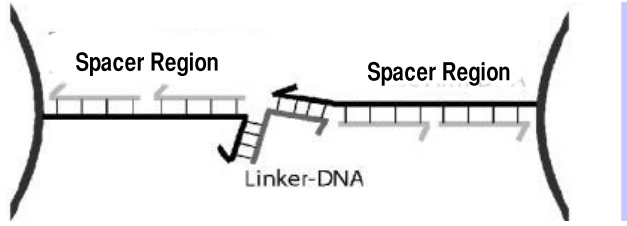


Figure 1.5: A schematic of a ssDNA bond mediated by linker DNA. The spacer region uses double stranded DNA (dsDNA) to enhance the stiffness of the DNA link. The ssDNA end connect to the linker DNA, which in turn connects to the ssDNA end of the other NP. Picture from ref. [29]

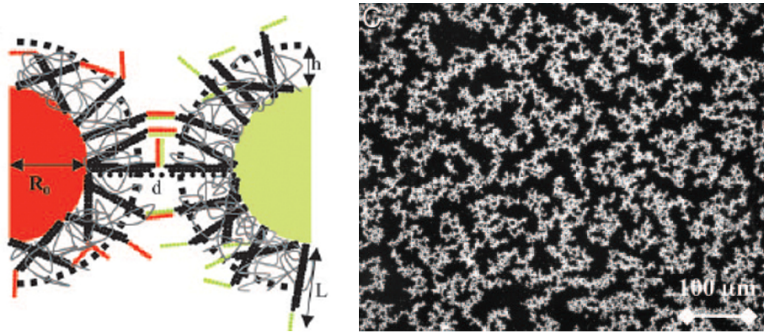


Figure 1.6: **Left:** Micrometer-sized colloids grafted with 61-bases oligonucleotides [26]. The system was observed to form self-assembly amorphous aggregates. **Right:** The amorphous aggregates formed by colloids in the picture on the left.

core using gold atoms with uniform coating of ssDNA was also experimentally realized (Fig. 1.7) [34]. While there has been success making ordered crystal structures [28, 30, 36, 37], such uniform coating makes it difficult to control the organization of higher order structures. In fact, both the aforementioned micrometer-sized colloid and gold-NP formed disordered assemblies [26, 34] (Fig. 1.6, right). If one can make an appropriate choice of geometry of the ssDNA attached to a core NP, or alternatively control the geometry of pre-assembled DNA macromolecules (*e.g.* the Holliday junction or synthetic junctions [38, 39]), it should be possible to control the symmetries of the resulting structures [24].

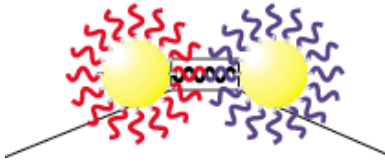


Figure 1.7: DNA-linked gold nanoparticles, which was observed to self-assemble into amorphous aggregates [34].

Such controlled attachment points to a core NP have been achieved experimentally. McLaughlin and coworkers [40, 41] successfully synthesized metal-ligand complexes as nano-hubs, which are tethered with 4 and 6 strands of oligonucleotide. While the experiment explicitly controlled the number of attached ssDNA (4 and 6 strands), the central ligand complexes in both 4 and 6-functional cases have a ring-like geometry, and therefore does not directly correspond to tetrahedral or octahedral coordination. In this case, the only way to achieve the desired tetrahedral or octahedral symmetry is through the negative charge repulsion between oligonucleotide strands, as oligonucleotide is negatively charged, or polyanionic. Ideally, this repulsion between tethered ssDNA should lead to a largely sterically tetrahedral or octahedral coordination. McLaughlin and coworkers, however, could not determine whether the self-assembled aggregates of this discretely functionalized NP are periodic or amorphous.

Another group lead by Alivisatos took a different approach to create discretely functionalized NP [42, 43]. Instead of specifying the coordination number of the central hub, the Au NP, Alivisatos *et al.* controlled the DNA:Au ratio, which determines the *average* number of DNA strands per particle (the valency). In this approach, the terminal thiol on the oligonucleotide binds to Au NP via a statistical process, which results in a distribution of functionality, *i.e.* the number of attached DNA. To obtain a specific functionality from this resulting distributional functionality, Alivisatos *et al.* employed two purification methods. The study shows that researchers successfully isolated Au NP functionalized with 0-5 ssDNA separately. However, because the binding of ssDNA to Au NP is through a random statistical process, there is still a lack of specification

on orientation of the tethered ssDNA.

NP functionalized with specific number of ssDNA, *i.e.* valency, and orientation is believed to be the key for nanocrystal development. However, due to experimental difficulties, such NP has not been fully realized: both McLaughlin and Alivisatos' group could only control the valency but not the orientations. There are also challenges in determining the structure of self-assembled aggregates from these NP with specified valency. To address the physical properties of this future material, we resort to computer simulations to investigate both the structure and dynamic of a model of NP functionalized with specified number and orientation of ssDNA (see chapter 2). Our results will potentially provide insight for future development of the DNA-functionalized materials.

1.3 Phase Behaviors of DNA-Functionalized Nanoparticles

A recent work studying a simple model for nanoparticles functionalized with four ssDNA in tetrahedral orientation (see chapter 2) demonstrated a rich phase behavior that has been rare in traditional materials [19]. The study discovered four thermodynamically distinct amorphous phases, separated by three amorphous phase transitions, unprecedented for a pure material. The three phase transitions are each terminated by a critical point, and all three critical points are found to be part of the Ising universality class like the ordinary gas-liquid critical point. These results indicate that the homogeneous system of the tetrahedrally-coated DNA NP is able to make at least four distinct liquids that are analogous to a gas state (which corresponds to the state of unassociated NP) and three additional liquid states (which corresponds to the networked fluid states of the NP).

To explain this unusual phenomenon, it is important to point out that, unlike uniformly

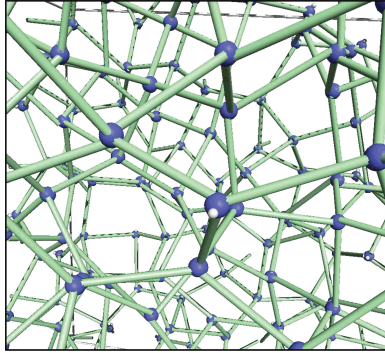


Figure 1.8: A cartoon visualization of a single network created by NP functionalized with 4 ssDNA in tetrahedral coordination. The blue spheres represent NP core, and the green tubes represent the dsDNA bond. Due to the long dsDNA linkage, there is significant empty space in the network evident in the picture. Image from ref. [19].

functionalized NP, the DNA-functionalized nanoparticles have limited bonding sites, or valency, and thus readily form a homogeneous low-density state with significant empty space in the network [44]. NP with a specified number of attached ssDNA (*i.e.* valency) can have near vanishing densities, since the length scale of the DNA bonding “arms” can be large as compared with the core NP size ($\approx 0.7 - 1$ nm), even when the length of the DNA sequence is below the dsDNA persistence length (≈ 50 nm). A cartoon visualization of this low density state due to the dsDNA linkage is shown in Fig. 1.8.

For the case of tetrahedrally functionalized NP, the units can assemble into a large scale amorphous network with locally tetrahedral order [17–19]. Moreover, since vast empty spaces exist and are locally tetrahedral, it is possible to repeat the motif with a second locally tetrahedral network occupying the unoccupied space of the first network (Fig. 1.9 left). Within the investigated length of the DNA sequences (less than 16 base pairs, $\approx 5 - 6$ nm), this process can be repeated a third time (Fig. 1.9 right), and at low temperature, these networked states become thermodynamically distinct phases, resulting in a phase diagram with 3 critical points and 4 amorphous phases. This multiplicity

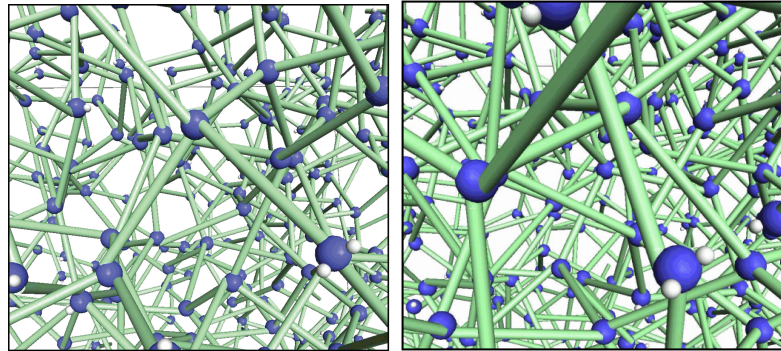


Figure 1.9: A cartoon visualization of two and three interpenetrating networks created by NP functionalized with 4 ssDNA in tetrahedral coordination. The empty space in the network created by long dsDNA linkage allows a second (left picture) and a third (right picture) network form and interpenetrates the first one. Image from ref. [19].

of amorphous phases is referred to as “polyamorphism,” [45] in analogy to “polymorphism,” the multiplicity of ordered crystal phases, such as occurs in many networked crystals like water and silica, as well as in certain classes of ultra-soft materials like star polymers [46]. The liquid-liquid phase transitions have also been found experimentally in phosphorus [47] and are suspected for many tetrahedrally coordinated fluids including water [48–53], carbon [54], silica [55, 56], and silicon [57]. It is argued that interpenetration of networks can be a general mechanism to liquid-liquid phase transition, leading to the phenomenon of multiple liquid in various materials [58].

Since the emergence of polyamorphism in the tetrahedrally functionalized NP is a consequence of the possibility to repeat interpenetrating tetrahedral structures, it is natural to ask whether such interpenetration can be effective when the network structure does not have a regular, repeating form. In this thesis work we explore a model of NP functionalized with 3, 5 or 6 ssDNA with various directional arrangements of DNA arms (see chapter 2). We present our findings in chapter 3 and 4.

1.4 Theory of Crystallization Process

In contrast to the amorphous self-assembled systems, the highly organized nano-crystals can potentially open up kaleidoscopic applications. One instance is to use three-dimensional DNA crystals as a scaffold to organize biological macro-molecules and assist the examination of the structures of the molecules [6]. The same scaffolding can also apply to building nanoelectronic components in two- or three-dimensional arrays [5]. To achieve these applications, the first step is to obtain a good control of crystallization in self-assembly materials. However, creating crystalline arrays of DNA-linked NP has proved challenging, though there have been some recent successes [27–31, 36, 37]. More frequently, the NP assemble into disordered aggregates [27, 33, 35, 59–62]. It is therefore valuable to understand the dynamical pathways the system must follow in order to crystallize, as well as the mechanisms that hinder this process.

To put these difficulties in the context of more traditional materials, we note that experiments on colloidal particles, which isotropically interact with each other, are well-known to exhibit a two-step crystallization mechanism. In these cases, the gas-liquid coexistence curve is metastable relative to the gas-solid coexistence curve. Quenching this system inside the gas-liquid coexistence region results in (i) a phase separation into a high density liquid, followed by (ii) crystal nucleation within this high density droplet. Quenching this system to much too low a temperature causes it to simply form disordered gels, thereby kinetically hindering crystal formation. There are considerable theoretical and simulation evidences for this scenario [63–72]. Similar ideas have also been proposed for proteins, and it is now believed that there is a “crystallization slot” outside which crystallization does not occur [66, 67, 73, 74].

An alternate scenario has also been proposed for the case of proteins interacting through strong, but patchy interactions: it has been argued that self-assembly, driven by highly specified local geometry imposed by the bonding sites, can create a locally high-density region which enhances the formation of nuclei, even in the absence of the thermodynamic

drive for phase separation. This two-step mechanism, mediated by this self-assembled gel state, is thus another pathway by which proteins can crystallize [64]. While the factors controlling the crystallization of colloids and proteins (or patchy colloids) thus seem to be system specific, we stress that crystallization in these soft matter systems always seems to follow this two-step kinetic scheme.

Even though the two-step mechanism seems universal in traditional materials, this general mechanism has yet been addressed in the context of homogeneous system with complex interparticle interactions such as the system of DNA-functionalized nanoparticles. In this thesis we use the computer simulation to examine the crystallization dynamics of the crystallizing DNA NP with respect to the two-step mechanism pathway. Furthermore, since DNA-functionalized NP are able to self-assemble to networked state, we can compare the possible two drives behind the process, namely, the effect of spinodal-assisted (*i.e.* phase separation driven) versus assembly-driven crystallization process. We present our results in chapter 4.

1.5 Study Objectives and Result Summaries

Even though simulation studies suggested that NP functionalized with ssDNA with specific number and orientation have unusual phase behaviors [19], to date the experiments has yet succeeded in making DNA-functionalized NP with controlled geometries in significant quantities (section 1.2). Specifically, simulations have shown that system of NP tethered with 4 ssDNA in tetrahedral geometry exhibits multiple amorphous phases, or polyamorphism, through constructing interpenetrating networks. However, it is not clear whether in systems of NP functionalized with other geometrical ssDNA, the polyamorphism phenomenon is still viable and, if yes, what mechanism underlies such phase behaviors. **Therefore, we extend a model used in ref. [19] to examine the phase behaviors of four other geometries: one 3-functional NP, two 5-functional NP with different geometries, and one 6-functional NP with 6**

ssDNA in octahedral orientation. We summarize our results in two points:

- **Amorphous Systems: 3-functional NP has one amorphous phase transition, while both 5-functionalized NP exhibit two phase transitions, a polyamorphism arised from interpenetrating of networks.**

For the 3-functional NP, we find only one single phase transition associated with two amorphous phases, analogous to traditional materials. Interestingly, we find that both of the two geometrically different 5-functional NP are polyamorphic: the system can undergo two amorphous phase transitions and construct three amorphous phases, even though one of the two geometries does not have regular space-filling property. Like the 4-functionalized NP in previous study [19], the highest density phase consists of interpenetrating networks, demonstrating that regular symmetry is not a prerequisite for interpenetration to produce thermodynamically distinct phases. The width of the coexistence regions for all phase transitions increases consistently with increasing functionality [75].

- **Crystal Systems: 6-functional NP exhibit polymorphism through a hierarchy of up to six interpenetrating simple-cubic lattices.**

For the 6-functionalized NP with octahedral symmetry, the possibility of observing high density amorphous phases is preempted by the formation of ordered crystal phases. Due to the extreme softness of the potential combined with the directional interaction, we observe (at least) *six* distinct crystalline structures (*i.e.* polymorphism) consisting of up to six interpenetrating simple cubic (SC) lattices. This strong tendency to form crystalline states in the 6-functional NP suggests that the number and orientation of functional ssDNA are critical factors in designing bottom-up synthetic materials for nano-crystals. This point is clear when viewed in the context of other geometries: the 3-functional and two 5-functional NP only produce amorphous phases. Even the 4-functional NP with tetrahedral symmetry does not construct crystalline structure, as reported in ref. [19]. Future research may investigate which symmetries of DNA-functionalized NP are favorable for

crystal state and their potential polymorphism.

These crystallizing systems of 6-functional NP allow us to examine the two-step pathway mechanism exhibited in many traditional materials: the system first forms densified amorphous state, followed by an ordering process. However, so far this apparent universality in crystallization has received limited attention in the context of DNA-functionalized NP where complex interactions engender untraditional phase behaviors. Moreover, even though it has been reported that both phase separation and self-assembly can lead to the initial densification in crystallization, direct comparison of the two driving forces has yet been addressed. **Using the system of 6-functional NP, we can compare the effect of spinodal-assisted (*i.e.* phase separation driven) versus assembly-driven crystallization process. Furthermore, because of the polymorphic nature of the system, we can compare the crystallization in different crystal structures.** Our results are as followings:

- **The crystallization of all systems of 6-functional NP follow the conventional two-step pathway mechanism,** regardless of the driving forces (phase separation or self-assembly) or crystal structure (single SC lattice or double interpenetrating SC lattices). In other words, this crystallization mechanism is applicable in polymorphic and self-assembling materials such as the DNA-functionalized NP in our study. In this direction, further experimental verification is necessary to provide credibility to this application of the two-step mechanism in system of NP with specified ssDNA-tethered.

1.6 Organizations of the Thesis

The thesis is organized as follows:

- Chapter II introduces the model used in the simulation. We will discuss the detailed coarse-grained version and a simplified version using effective potential for

computation efficiency. Using this effective potential, we construct four other orientations of DNA tethers. The chapter ends with an overview of various simulation methods employed for different systems.

- Chapter III details our results for the amorphous states. In particular, we will trace out the phase boundaries for NP of three different orientation (3-TP, 5-TBP, and 5-SBP) and study their structures at high density regions.
- Chapter IV addresses both the equilibrium and dynamic aspects of the self-assembled crystals. We present the phase diagram for six different crystal lattices composed by the same DNA-coated NP (6-octahedral geometry). In terms of the dynamics, we found that the conventional “two-step” pathway mechanism for crystallization can be applied to the system of DNA-mediated assembling blocks.
- Chapter V is a general discussion on the mechanism of interpenetration, an overarching theme in amorphous and crystal systems of DNA-functionalized NP. We also relate the crystallization dynamics to other experimental works.
- Chapter VI summarizes the main points of this work and discuss the future perspectives.

Chapter 2

Model and Simulation Methods

In this chapter, we introduce the coarse-grained model for DNA-functionalized nanoparticles in section 2.1. Based on this detailed model, we develop an effective potential in section 2.2 to aid computation, which allows us to modify the number and orientation of tethered ssDNA in section 2.3 to study the valency and geometry dependence of phase behavior. We end the chapter with a brief overview of simulation methods in section 2.4.

2.1 Coarse-Grained Model

There exists a variety of models for DNA ranging from “atomistic” versions [76–78], which retain much of the chemical details, to crude bead-string description [79]. In order to provide a prediction of the three-dimensional self-assembled structures, we need a model that is computationally expedient to simulate large number ($\gtrsim 10^2$) of nanoparticles, yet still detailed enough to capture the key ingredients in DNA-mediated self-assembly. Therefore, we introduce a coarse-grained model for ssDNA schematically shown in Fig. 2.1 [17]. This model, which has also been adapted to describe complex DNA architectures like the Holliday junction [80], captures the base-pair selectivity

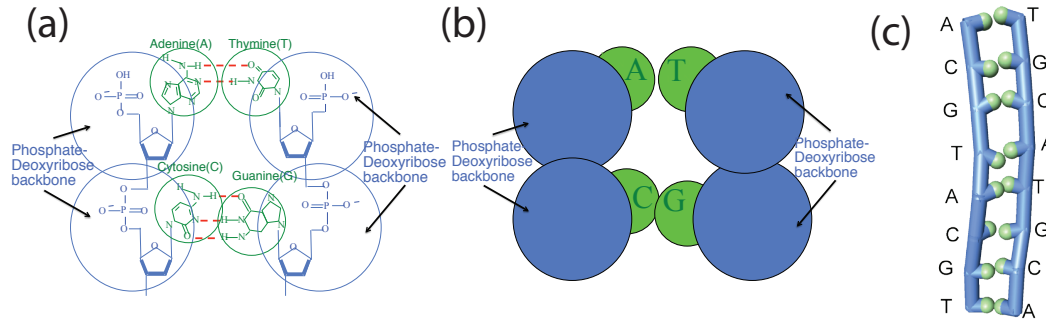


Figure 2.1: Schematic of the coarse-grained model of DNA. (a) shows the chemical details of the four bases (A, T, C, G). The structures of each base are concentrated into two force sites as shown in (b): a blue sphere representing the backbone, and a green “sticky spot” that has attractive interaction with a complementary base. (c) is an example of ssDNA which is self-complementary in reverse direction.

between two ssDNA and the bonding selectivity which ensures that each base can only bond to one other base. In detail, we represent ssDNA as a string of monomers (the blue sphere in Fig. 2.1 (b)) with “sticky sites” (the green sphere in Fig. 2.1 (b)) that serve as the bonding sites. Each sticky site only bonds to another sticky site with a complementary base type (A with T, C with G), and thereby preserves the Watson-Crick basepairing. Moreover, the small size of the sticky spot relative to the monomer backbone prevents a third sticky site from joining the existing bond, which ensures the one-to-one “lock-and-key” interaction between two ssDNA. Here we point out that our model does not include the electrostatic interaction. All spheres (or force sites) interact via a shifted-force Lennard-Jones (LJ) potential

$$V_{sf}(r) = V_{LJ}(r) - V_{LJ}(r_c) - (r - r_c) \frac{dV_{LJ}(r)}{dr} \Big|_{r=r_c}, \quad (2.1)$$

where the r_c is the cutoff distance at which the potential is truncated. For $r > r_c$, $V_{sf}(r) = 0$. $V_{LJ}(r)$ is the Lennard-Jones (LJ) potential

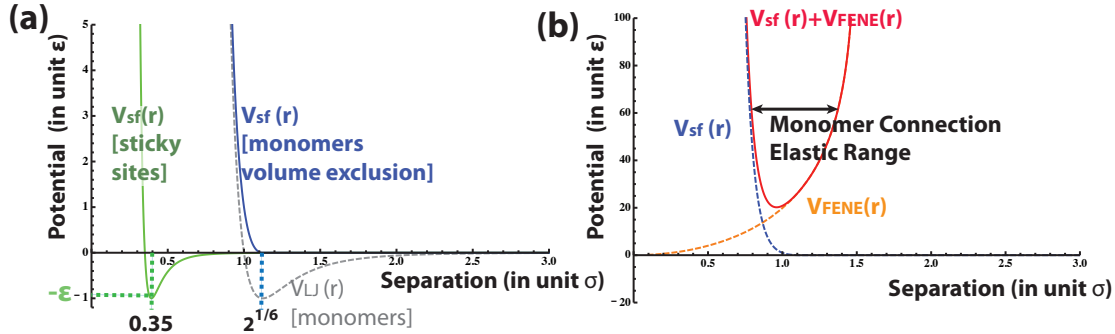


Figure 2.2: (a) Plots of Lennard-Jones potential $V_{LJ}(r)$ and shifted-force Lennard-Jones potential $V_{sf}(r)$. The light green curve represents the $V_{sf}(r)$ for complementary sticky sites, which preserves the attractive potential well; the blue curve is $V_{sf}(r)$ for monomer-monomer soft-core repulsive potential. The dashed gray cuve is the (original) $V_{LJ}(r)$. (b) shows the combination of FENE potential with $V_{sf}(r)$ that together limit the connected monomers to a certain separation (the black arrow).

$$V_{LJ}(r) = 4\epsilon \left[\left(\frac{\sigma}{r} \right)^{12} - \left(\frac{\sigma}{r} \right)^6 \right], \quad (2.2)$$

where ϵ is the depth of the potential well, corresponding to the energy of a single basepair bonding (Fig. 2.2 (a)) and the length is in unit $\sigma = \sigma_{m,m}$, where $\sigma_{m,m}$ is the diameter of the monomer. For the smaller sticky sites, $\sigma_{s,s} = 0.35\sigma_{m,m}$. By choosing $r_c = 2^{1/6}\sigma$ near the bottom of the potential well, we can have purely repulsive interaction (Fig. 2.2 (a) blue curve). This repulsive potential captures the volume exclusion of each force site. For the sticky sites, however, $r_c = 2.5\sigma$ between complementary bases and the potential well is preserved to capture the hydrogen bonding of the DNA basepairing (Fig. 2.2 (a) green curve).

To string the monomers together and connect it to the hub, we employ a finitely-extensible, nonlinear elastic (FENE) potential

$$V_{\text{FENE}}(r) = -\frac{kR_0^2}{2} \ln \left[1 - \left(\frac{r}{R_0} \right)^2 \right], \quad (2.3)$$

where $k = 30$ is the bond strength and $R_0 = 1.5$ denotes the maximum bond extension (Fig. 2.2 (b) orange curve). Combined with LJ potential, $V_{\text{FENE}}(r) + V_{sf}(r)$ connects the monomers elastically within a small range (Fig. 2.2 (b) black arrow).

The characteristic rigidity of the DNA strands is modeled by a three-body potential

$$V_l = k_l(1 - \cos \theta), \quad (2.4)$$

, where θ is the angle defined by three consecutive monomers. $k_l = 5$ allows for moderate flexibility but still prevent worm-like entanglement of the DNA strands. Finally, we point out that the only interactions in this system are between the bonding arms and repulsive NP cores, and the NPs themselves are in an athermal solvent.

2.2 Effective Potential Model

This detailed model of base-base interaction is computationally costly for studying the bulk behavior, due to the large number of force sites required. For example, a bonding of just two tetrahedral NP functionalized with 8-base ssDNA involves 136 force sites (Fig. 2.3 A). Therefore, an effective potential model was introduced to simplify the original model [81]. This effective bonding potential between two ssDNA arms parameterizes the interactions of the original model using only the separation of the two nanoparticle cores and the relative angular orientation defined by the position of the DNA arms (Fig. 2.3 C and D). Here we briefly describe the procedure employed to obtain this effective potential.

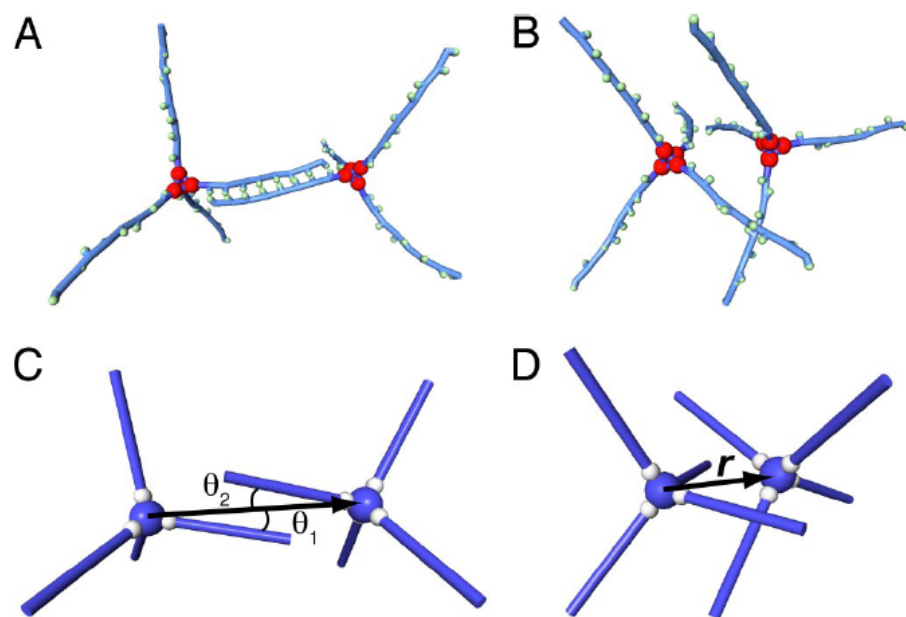


Figure 2.3: Schematic of the parametrization of the coarse-grained model. C and D are visualizations of A and B in the effective potential model. The effective potential considers only (i) the relative angles of the ssDNA arms with respect to the axis through two cores (indicated in C), and (ii) the core-core separation r (indicated in D).

The effective potential for a given set of parameters ($V(r, \theta_1, \theta_2, T)$, where r and θ_1, θ_2 are defined in Fig. 2.3 C, D) are obtained by a systematic study of the coarse-grained model. At any temperature and density, we can numerically evaluate the probability $P(r, \theta_1, \theta_2)$ of finding a pair with relative relative orientation (r, θ_1, θ_2) . From statistical mechanis, we know this must be related to a Boltzmann factor. In the canonical ensemble,

$$P(r, \theta_1, \theta_2, T) \propto e^{-\beta V(r, \theta_1, \theta_2, T)}. \quad (2.5)$$

By inverting this relation, we obtain the effective $V(r, \theta_1, \theta_2, T)$. Through a series of simulations of two DNA-functionalized NP in a box, ref. [19, 81] extracted the angular and radial pair correlations at two temperatures: a low temperature, where essentially all simulations of a pair NP equilibrated to bonded state, and a high temperature, where all simulation of a pair NP equilibrated to unbonded state. At each T , the radial component of V is numerically determined, while the angular portion can be well described by a Gaussian function

$$P(\theta) = \frac{1}{\sqrt{2\pi}\sigma^2} e^{-\theta^2/2\sigma^2}. \quad (2.6)$$

The studies showed that for all intermediate temperatures, the angular and radial pair correlations can be accurately interpolated from correlation data at the two investigated (extreme) temperatures. This success is peculiar to the DNA system, because the DNA bonding is highly sensitive to temperature, and therefore temperature alone effectively captures the change of pair NP bonding probabilities in both the radial and angular components. The interpolation to intermediate tempreature by combining the bonded (low temperature) and non-bonded (high temperature) states, however, requires a combination weight, which is the *general* bonding probability of a pair NP ($P_b(T)$) at that intermediate temperature. This probability can be calculated from a two-state (bonded and non-bonded DNA) model

$$P_b(T) = \frac{1}{\left[1 + \exp\left(-\frac{\Delta U - T\Delta S}{k_B T}\right)\right]}, \quad (2.7)$$

where ΔU and ΔS are the change in energy and entropy associated with the formation of a double strand. The study showed that this model nicely fits the coarse-grained simulation data. Combining expression for $P_b(T)$ and V at low and high T , we are able to obtain the radial and angular bonding probability (and, from equation 2.5, the associated potential) at *all* temperatures. In conclusion, the pair-wise bonding probability is readily parametrized by angular and radial separations, both of which can be constructed from data at one high and one low temperatures with a weight calculated from a two-state model.

These bonding probabilities can in turn be used to build the effective potential via statistical techniques. To preserve the 1-1 bonding of ssDNA, we superimpose an additional lock-and-key condition. This is done by keeping track of the availability of each bonding site, which allows us to explicitly exclude any attractive interaction between a bonded (unavailable) ssDNA to other DNA. The studies showed that this parameterized effective potential quantitatively reproduced the structure and phase behavior of the coarse-grained model of NP functionalized with four ssDNA in a tetrahedral orientation [19, 81]. It has been verified that the effective potential model quantitatively reproduces the behavior of the coarse-grained model in phase behaviors, structural factors $S(q)$, and radial distribution $g(r)$ [81]. Further details of the construction of effective potential are described in the thesis of Chia Wei Hsu.

2.3 Studied Variations of Geometry

We use this this effective non-additive pair potential as a starting point, and use the same form of the effective potential between DNA strands. To examine the effect of valency, we consider several choices for the number of ssDNA tethered to the nanoparticle

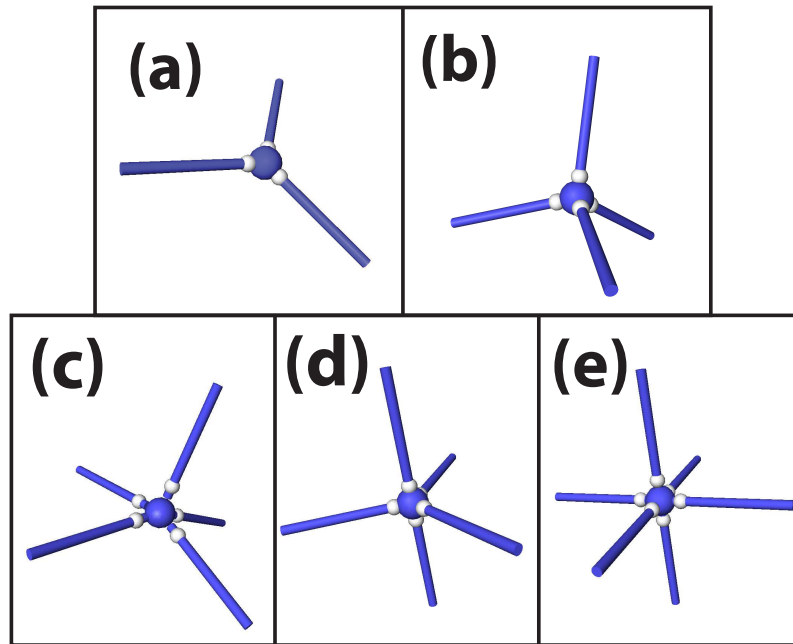


Figure 2.4: Cartoon of the geometries of the DNA functionalized nanoparticles studied: (a) 3-functional triangular planar (3-TP), (b) tetrahedral, (c) 5-functional square-based pyramid (5-SBP), (d) 5-functional triangle-based bi-pyramid (5-TBP), (e) octahedral. The central sphere indicates the NP, while the cylinder represent the sequence of DNA base pairs tethered to the central core at the small sphere locations.

cores. Previous theoretical studies show that 2-functional NP form chains and do not exhibit phase transition [82, 83]. The 4-functional case has been examined in ref. [19]. Furthermore, for large number of ssDNA, the effect of limited valency decreases and the phase behaviors quickly converge to regular spherical potential [83]. Based on these considerations, we choose NP functionalized with three to five ssDNA, with distinct geometries. The DNA length was fixed to four bases. Figure 2.4 summarizes the geometries of the DNA-functionalized NP we study: (a) the 3-functional triangular planer (3-TP) are tethered with three ssDNA geometrically distributed on the same plane, 120° apart pairwise; (b) the tetrahedral geometry resembles the bond orientation of a carbon atom in a diamond lattice; (c) the 5-functional square-based pyramid (5-SBP) structure has five ssDNA pointing to five vertexes of the square-based pyramid; (d) the 5-functional triangle-based bi-pyramid (5-TBP) has the shape of sp^3d hybridized orbitals, equivalent to adding two additional ssDNA perpendicular to the previous 3-TP geometry; (e) the octahedral unit aligns six arms along orthogonal axis. The tetrahedral geometry has been discussed previously [19]; here we focus our attention on the other four geometries to investigate the valency dependence of phase behavior.

The phase diagram corresponding to geometries (a)–(d) will be discussed in chapter 3, while the behavior of the octahedral units will be discussed in chapter 4.

2.4 Simulation Methods

For the amorphous systems in chapter 3, we first perform a series of Monte Carlo simulations in the grand canonical ensemble (fixed chemical potential μ , volume V , and temperature T) to coarsely map out the phase diagram from isotherms in the density–chemical potential ($\rho - \mu$) plane. Here we use reduced units defined by the effective potential [81]. Discontinuities of ρ indicate the approximate phase boundaries of a first order phase transition. These results serve as a guide for more refined calculations, which we describe in the following.

To accurately locate the critical point, we select a state point that exhibits a bimodal density distribution $P(\rho)$, as $P(\rho)$ is known to be bimodal close to a second order critical point. Moreover, since the order parameter distribution $P(M)$ at the critical point for our system should follow the Ising universality class [19], we apply a histogram reweighting scheme [84] to estimate the critical temperature T_c and critical chemical potential μ_c where $P(M)$ takes the expected form. Here $M = \rho - su$; u is the potential energy density and s is the field-mixing parameter. We carry out an additional simulation at the estimated T_c and μ_c , and refine the estimate of T_c and μ_c again from histogram reweighting. We iterate this process until $P(M)$ converges to the form of the Ising class to within a very narrow tolerance.

Starting from the critical point and going down in T , we calculate $P(\rho)$ at phase coexistence using multicanonical sampling to *preattend* the sampling and artificially enhance the occurrence of switching between coexisting phases [84]. This requires that we first use histogram reweighting again to determine the appropriate μ for phase coexistence when we change T . The initial estimate for μ may require further refinement after performing an initial simulation. The densities of the coexisting phases can then be determined from the peaks of the $P(\rho)$ distribution at coexistence.

For the crystallizing system in chapter 4, we study the model via Monte Carlo (MC) simulation in the canonical ensemble (fixed number of particles N , volume V , temperature T). To describe the crystallization dynamics, we use Monte Carlo steps (MCS) as the time unit. Monte Carlo steps are associated with the number of Monte Carlo updates: for a randomly chosen NP, we perform three sequential attempts – (i) NP translation without rotation, (ii) NP rotation without translation, and (iii) a combined NP translation and rotation. We define one Monte Carlo step (MCS) as N such attempts, where N is the total number of NP. For reference, the total computational time for our study is estimated to amount to ≈ 25 months.

Chapter 3

Amorphous Systems

The ability to form amorphous aggregates is the first sign of self-assembly. So far virtually all DNA-mediated self-assembly systems exhibit an amorphous dense phase (for example, Fig. 1.6, right). In addition , the reversibility upon the heating and cooling cycle is another important evidence to demonstrate that the self-assembly is mediated by DNA, which can dehybridizes and hybridizes at different temperatures. Some experimental systems, however, do not have this second characteristics [85, 86]. Here we report that all our modeled systems readily form large amorphous aggregates given appropriate density and temperature. These systems are also reversible at changing temperatures, demonstrating that the aggregates self-assemble via forming dsDNA [75]. In this chapter we take the advantage of simulation to closely examine the phase behaviors (Section 3.1) and the associated morphologies and structures (section 3.2). We will further discuss the implications of our results in chapter 5.

3.1 Phase Behaviors

We evaluate the phase behavior using the numerical procedures described in chapter 2 and locate the phase boundaries in the $(T - \rho)$ plane for the 3-TP, 5-TBP, and 5-SBP

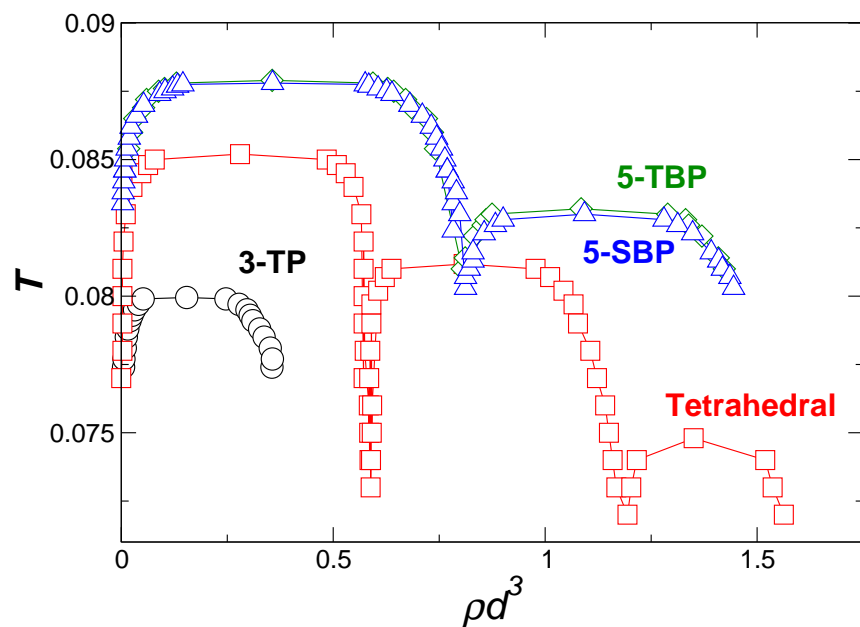


Figure 3.1: $T - \rho$ phase diagram of geometries 3-TP, tetrahedral, 5-TBP, and 5-SBP. The density is scaled by the bonding distance d^3 such that the density is comparable to the density of hard-sphere systems.

complexes (Fig. 3.1), and include data for the tetrahedral dendrimer previously studied for comparison [19]. We find that 3-TP systems exhibit only one phase transition between unassociated molecules and a networked fluid state, analogous to a gas-liquid phase transition. We cannot formally rule out an additional phase transition at $T \leq 0.07$ (the lowest T investigated), but we do not expect any additional transition based on the relative transition temperatures for the 4 and 5-armed systems, which we now examine.

Both the 5-SBP and 5-TBP systems exhibit two critical points and three amorphous phases, as in the tetrahedral system, which has one more critical point and phase than the 5-armed systems. Simulations at larger ρ and low T for systems of both 5-armed nanoparticles show a rather sharp crossing between two states of different ρ , but we were unable to uncover unambiguous evidence that this crossover is discontinuous (i.e., not an additional first-order transition). In the previous study of the tetrahedral system, the occurrence of multiple critical points was explained by the formation of multiple interpenetrating networks [19]. Our results indicate that multiple phase transitions can also occur for other geometries. But the question remains: do the multiple transitions occur in the 5-armed systems by constructing interpenetrating networks, or by some other means. We will address this question in the next section examining the structure.

The locations of the critical points of both the gas-liquid and liquid-liquid phase transitions decrease in both ρ and T as the valency decreases, and coexistence regions become smaller. These results are in agreement with previous findings for the liquid-gas transition of systems with limited valency γ [44, 87]. To our knowledge, this is the first time the effect of valency on the liquid-liquid transitions has been examined. The decrease of T_c with decreasing γ can be understood from the fact that, with fewer bonding arms, the total binding energy of a networked state is smaller. Accordingly, less thermal energy is required to break up the network into a gas-like phase. The decrease of ρ_c with decreasing γ can be understood from the fact that, with fewer bonding arms, fully bonded structures require lower densities. Furthermore, the decrease of density for low valency

particles was suggested to provide an equilibrium route, as opposed to phase separation [71], to gel formation in the context of short-range particle interactions [83, 88]. This work demonstrates that a strong thermodynamic driving force for phase separation — competing with the formation of equilibrium gels — may be present even for densities larger than the gas-liquid typical densities when the softness of the potential allows for formation of interpenetrating fully bonded networks via the onset of additional phase separations. Moreover, our results suggest that this unexpected phenomenon does not require a specific valence or a specific orientation, and can be exhibited by nanoparticles with more complex interactions.

The two geometries with $\gamma = 5$ exhibit phase boundaries that are nearly quantitatively identical, indicating that the phase behavior is surprisingly insensitive to geometric differences of the molecular units we have studied. This result agrees with previous study of systems of hard-sphere patchy particles with either fixed or random location of the patches [44]. However, in the patchy hard sphere system — where nearest-neighbor distances are controlled by the hard-core diameter and not by the bonding — only one phase transition is observed. If binding can occur in any direction, it will be possible to form all bonds at nearly any liquid-like ρ . With specific orientation of the arms, not all bonds may be possible in some density ranges, potentially creating a thermodynamic drive to separate into coexisting phases which are each fully bonded. In other words, the specificity in distances and orientations required for bonding introduces a strong coupling between the energy of the system and its density, thus establishing optimal density values where fully bonded states can be achieved. This phenomenon is consistent with the results in ref. [89], where the thermodynamic drive due to the specified local geometry (of tetrahedral order) favors certain density and causes anomaly in dynamics near this density. Such tendency to form network at favorable density, however, did not result in the onset of additional phase separation as the double interpenetrating amorphous network in our system.

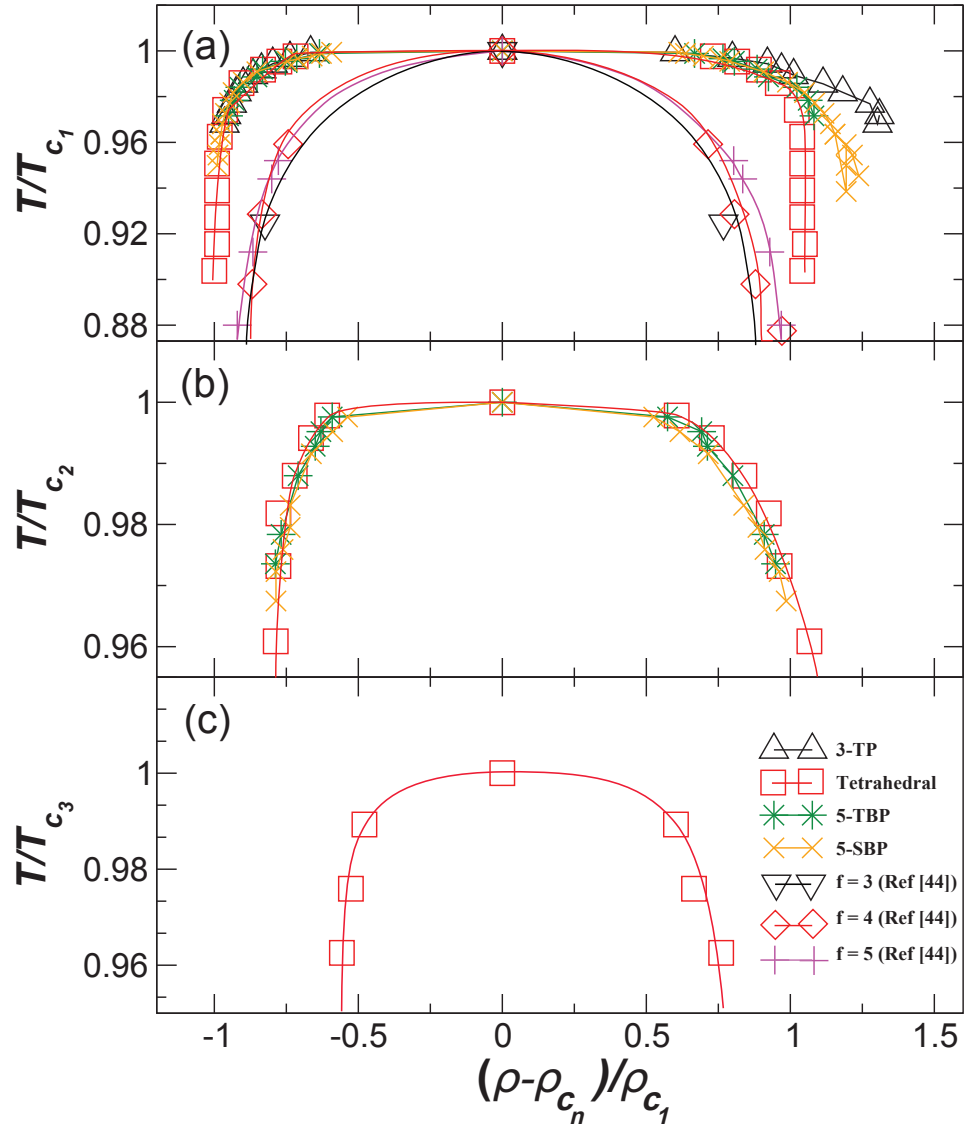


Figure 3.2: $T - \rho$ phase diagram with density shifted by respective critical densities and scaled by first critical density; the temperature is scaled by the respective T_c . The solid lines are guides to the eye. (a) The first phase transition, analogous to a gas-liquid transition, for geometries 3-TP, tetrahedral, 5-TBP, 5-SBP. In addition, we show results from patchy colloids from reference with either 3, 4, or 5 patches [44]. (b) The second phase transition, a liquid-liquid phase transition, for geometries 5-TBP, 5-SBP, and tetrahedral. (c) The third phase transition for tetrahedral geometry.

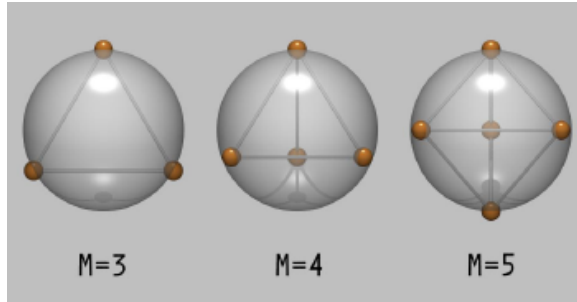


Figure 3.3: Schematic representation of the location of the “sticky patches” (centers of the small spheres) on the surface of the hardcore particle. The lines between different interaction sites are drawn only to help visualize the 3-D geometry. See ref. [83]

3.1.1 Valency Dependence of Phase Boundaries

Since the phase boundaries in our systems is insensitive to the local arrangement of ssDNA, it is convenient to discuss the valency dependence of phase behaviors. To assess how the shape of the coexistence curves depends on valency, we examine a scaled version of the phase diagram in Fig. 3.2. Specifically, we first scale T by the respective critical temperature of each transition. We then shift ρ by ρ_c for each transition separately. We also scale the density of each transition by critical density of the first phase transition so that the widths of the coexistence regions are comparable. Results from reference [44] are also added to Fig. 3.2(a) to facilitate the comparison of the phase boundary of the ssDNA-armed nanoparticles with that of the colloids functionalized with three, four, or five geometrically distributed “sticky patches” that serve as bonding sites (Fig. 3.3) [44, 83].

For the DNA system, the shape of the liquid-gas phase boundary near T_c is largely insensitive to the number of arms (Fig. 3.2(a)). Further from the critical point, the 3-armed system appears widest, consistent with the patchy colloid system (although the difference in width for the patchy colloidal system occurs further from the critical point, outside our plot range. See Fig. 3.4.) The phase boundary for the second transition (in the 5-TBP, 5-SBP, and tetrahedral systems) appears largely insensitive to the number

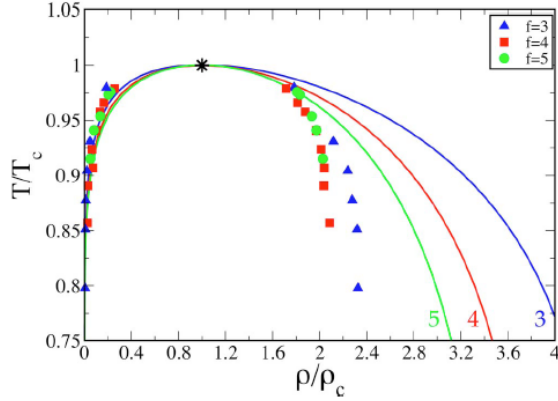


Figure 3.4: Gas-liquid coexistence curves of a previously studied model with limited valency [83]. The diagram uses reduced temperature T/T_c and the reduced density ρ/ρ_c for systems with $f = 3, 4, 5$ “sticky patches” [83]. Here we only compare with the simulation results (dots), which we reproduce in Fig. 3.2(a). The lines are theoretical prediction that we do not consider.

or orientation of the arms. However, we should be careful to point out that our data for the phase boundaries of DNA-functionalized NP only cover a small range near the critical point; further from T_c , the phase boundaries may differ. For reference, we also show the third transition for the tetrahedral system (Fig. 3.2(c)).

We note that there is a clear difference in phase boundaries of the DNA and patchy colloid systems, which can be explained by the nature of DNA bonding. In our model, the DNA arm bonding process requires simultaneous bonding of a sequence of four DNA bases. This high degree of cooperativity in bonding yields a much larger entropy change on bonding than for the patchy colloids. Accordingly, the phase separation occurs over a very narrow window, flattening the phase boundary near the critical point.

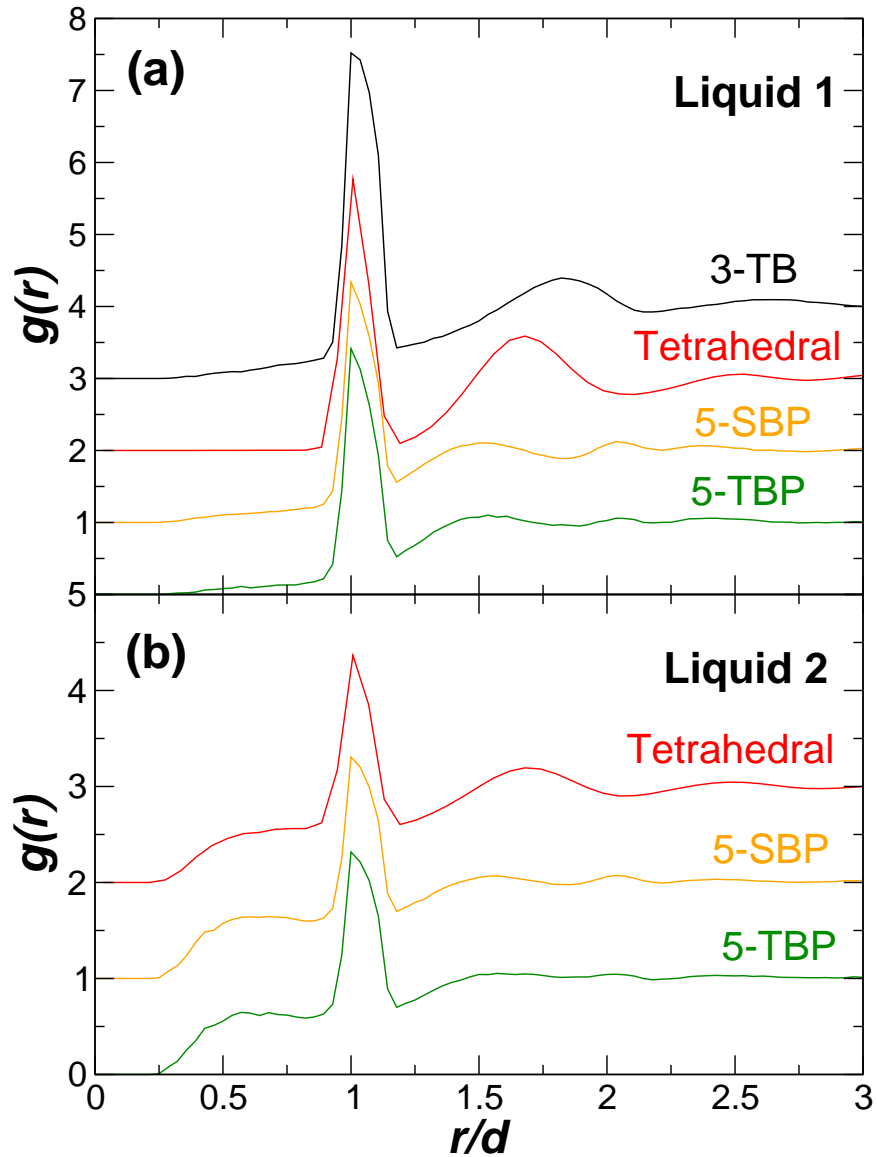


Figure 3.5: The radial distribution function $g(r)$ as a function of scaled distance r/d , where d is the typical bonding distance. For visual clarity, $g(r)$ for 5-SBP, tetrahedral, and 3-TB are shifted vertically by 1, 2, and 3 respectively. (a) $g(r)$ of the first liquid, including geometries 3-TB ($T = 0.08$, $\rho d^3 = 0.28$), tetrahedral ($T = 0.073$, $\rho d^3 = 0.64$), 5-SBP ($T = 0.0826$, $\rho d^3 = 0.86$), and 5-TBP ($T = 0.0825$, $\rho d^3 = 0.82$). (b) $g(r)$ of the second liquid, including tetrahedral ($T = 0.073$, $\rho d^3 = 1.29$), 5-SBP ($T = 0.0826$, $\rho d^3 = 1.43$), 5-TBP ($T = 0.08250$, $\rho d^3 = 1.44$.)

3.2 Structure

3.2.1 Pair Correlation Function

It remains unclear how the 5-armed NP, one of which can not build a regular space filling geometry, form one gas phase and two networked liquid phases. Therefore, we examine the fluid structure to determine if the second phase transition in the 5-SBP and 5-TBP systems arise through network interpenetration, as previously shown for the tetrahedral system. As a first step in this direction, we calculate the radial distribution $g(r)$, where r is the separation between the centers of particles. We show $g(r)$ for the first networked liquid (*i.e.* for the phase coexisting with the gas) for all geometries in Fig. 3.5(a); we show $g(r)$ for the second network liquid for the tetrahedral, 5-SBP, 5-TBP systems in Fig. 3.5(b). The separation r is scaled by d , the typical bonding distance, so that the first peak (the separation of the first bonded neighbor) is at $r/d = 1$. For the tetrahedral system, the second-neighbor peak occurs at $4/\sqrt{6} \approx 1.63$ times the position of the first-neighbor peak, typical for an ideal tetrahedral coordination. In contrast, $g(r)$ for the single network formed by 3-TP has a broader second peak at $r/d \approx \sqrt{3} \approx 1.8$, consistent with the 120° angle between two arms. For the 5-SBP and 5-TBP systems there is a very weak and broad second peak at $r/d \approx 1.5$. This clarifies that the 3 and 5 armed systems do *not* form networks with a locally tetrahedral order.

The structural difference between single networks of tetrahedral and the other geometries can also be observed in the region $r/d < 1$. Specifically, for the tetrahedral structure, $g(r)$ is identically zero for $r/d \lesssim 0.8$, while 3-TP, 5-SBP, and 5-TBP have a small amplitude for $0.25 \lesssim r/d \lesssim 0.8$, signifying the presence of molecules at distance closer than first-bonding neighbors. Accordingly, the structures of these networks are far less regular than the tetrahedral system.

For the second liquid of the polyamorphous systems (Fig. 3.5(b)), we observe a significant increase in $g(r)$ for the region $r/d < 1$. The large increase of particles at distances

less than the first-neighbor binding distance is consistent with the presence of a complementary network that interpenetrates the first one. Such interpenetration is possible due to the short range of core repulsion compared to the bonding distance. Structural features similar to those of the first liquid can be observed in the second liquid: the second peaks of tetrahedral geometries, 5-SBP, and 5-TBP occur roughly at the same positions as the first liquids of each geometry, but become slightly broader. The preservation of signatures of $g(r)$ suggests a similar structure of each of the interpenetrating networks.

3.2.2 Chemical Distance Analysis

To demonstrate that interpenetrating networks preserve their structure locally, we examine the $g(r)$ restricted to nanoparticles that are separated by a specific number of bonds, referred as chemical distance D (Fig. 3.6). More specifically, $g(r)$ for $D = 1$ only shows the correlations with the nearest bonded neighbors, while $D = 2$ includes both the first and second bonded neighbors, etc. In this way, we can calculate the correlation only among the bonded neighboring particles that are separated by no more than D bonds. The ordinary $g(r)$ is recovered in the limit $D \rightarrow \infty$.

The difference between the networks formed by the tetrahedral system and the two 5-armed systems is best demonstrated by examining $g(r)$ for $D = 2$. For the tetrahedral system, the second bonded neighbor has a well-defined peak position, determined by the tetrahedral network. For the 5-SBP and 5-TBP systems, $g(r)$ at $D = 2$ shows *two* distinct peaks for the possible location of the second bonded neighbor. This further demonstrates that these systems form a less sharply defined network than the tetrahedral system. Differences in the network geometries can also be observed in $g(r)$ for region $r/d < 1$. Since the restricted $g(r)$ only considers bonded neighbors, the increase at region $r/d < 1$ is a contribution from particles of the same network that loop back to very small physical distance r (but relatively large D). For tetrahedral networks, a

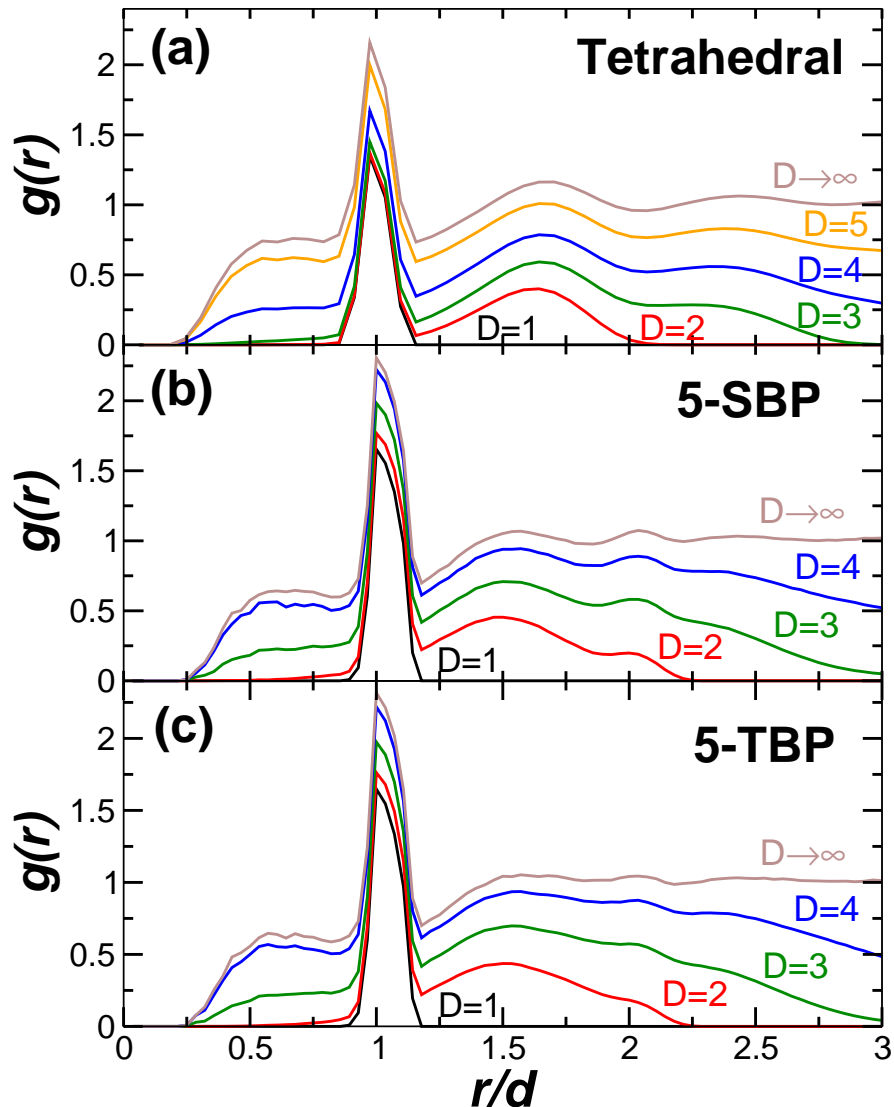


Figure 3.6: $g(r)$ restricted to bonded neighbors up to a specific chemical distance D for the second liquid of (a) tetrahedral geometry ($T = 0.073$, $\rho d^3 = 1.29$), (b) 5-SBP ($T = 0.0826$, $\rho d^3 = 1.43$), and (c) 5-TBP ($T = 0.08250$, $\rho d^3 = 1.44$.)

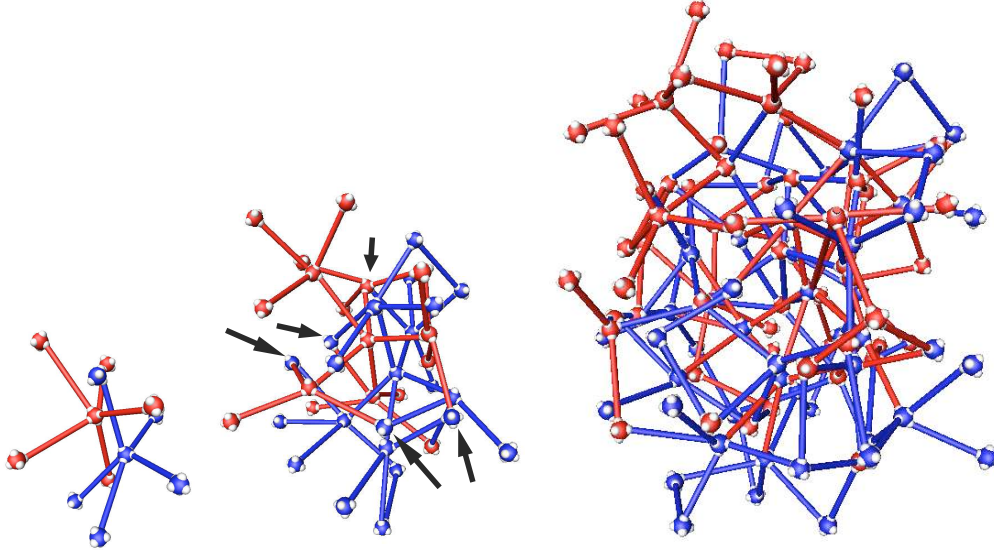


Figure 3.7: Visualization of two interpenetrating networks up to $D = 1$, $D = 2$ and $D = 3$ for 5-SBP at $T = 0.0826$, $\rho d^3 = 1.44$. We assign two different colors to illustrate the two distinct interpenetrating networks. The arrows indicate locations where the two networks intersect each other as a result of distortion.

significant increase of $g(r)$ at region $r/d < 1$ only occurs at $D \geq 4$, whereas for 5-SBP and 5-TBP systems, the increase takes place at $D \geq 3$. This shows that the 5-armed particles loops back more easily than the tetrahedral geometry, consistent with a more distorted network.

Finally, we can explicitly show the interpenetration by drawing two neighboring but disconnected DNA complex cores with the associated networks up to $D = 1$, $D = 2$, and $D = 3$ for a system of 5-functionalized NP at the region of high ρ and low T (Fig. 3.7). The two different colors indicate two interpenetrating networks. For $D = 1$, the two interpenetrating networks separate cleanly (Fig. 3.7(a)). However, when $D = 2$, two networks are connected at 5 points, indicated by the arrows. We can also observe a closed loop in the blue network on the top right in Fig. 3.7(b). The two networks are further distorted at $D = 3$. Some red NP are connected to multiple blue bonds, and vice versa, suggesting the interconnectedness of the two networks. Nonetheless, a large

portion of the two networks are distinct and can be easily identified at the local range. From the rapid growth of the entanglement, it is clear that the interpenetration of two networks is a local trait which loses sharpness at long range.

Chapter 4

Crystal Systems

While amorphous phases are common in self-assembled systems, crystal order is peculiar to a small subset of DNA-functionalized materials (section 1.2). In general, crystallization is still challenging in areas ranging from protein crystallography to self-assembling systems, and predicting which crystal structure will form under what circumstances is still largely an unsolved problem [90]. In this chapter, we demonstrate the rich crystal structures formed by the 6-fuctionalized octahedral NP (section 4.1). We further study the crystallization dynamics of these systems (section 4.3). Our results reveals insights to the question “Why is crystallization hard?” which we attempt to answer in chapter 5.

4.1 Phase Behaviors

Unlike the other geometries which make disordered networked states, the system of DNA complexes with octahedral geometry (Fig. 2.4(e)) readily forms an ordered crystal lattice. The octahedral geometry naturally lends itself to the formation of networks with cubic symmetry, as noted previously in studies of patchy colloids with six interacting sites [64, 91]. Our simulations indicate a transient amorphous phase is possible, but

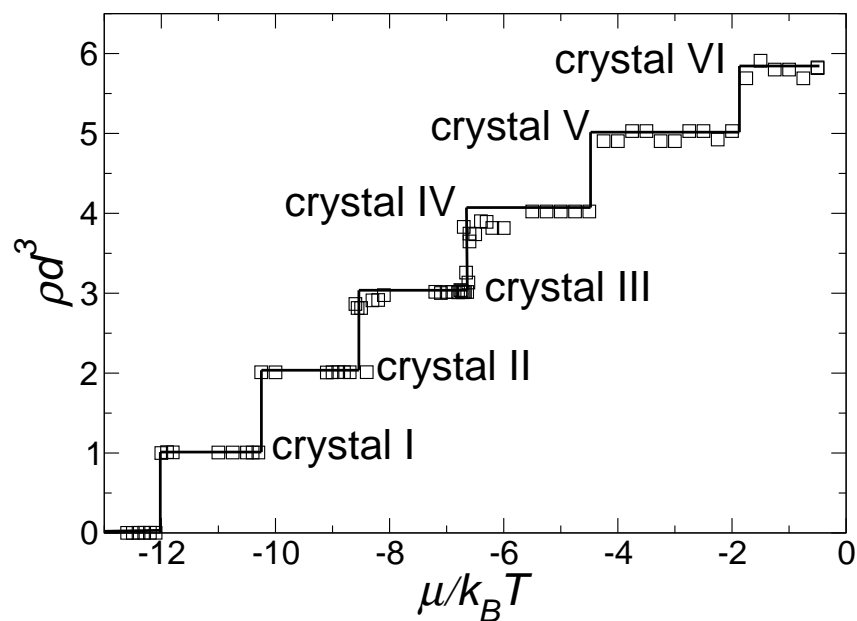


Figure 4.1: $\rho - \mu$ phase diagram of 6 crystals at $T = 0.08311$. The density is scaled by d^3 , where d is the typical bonding distance. The line is a guide to the eye.

it rapidly crystallizes. The lowest density crystal phase, which we call crystal I, has density $\rho d^3 = 1$. This cubic geometry has a complementary lattice of holes that is also cubic, which should allow for the possibility of interpenetrating crystal networks. Indeed, Fig. 4.1 shows that, by increasing μ at fixed T , we can observe a series of up to six thermodynamically distinct polymorphous phases. Each subsequent crystal has density equal to integer multiples of the density of crystal I, suggesting repetitions of the crystal I lattice. The visualization of each crystal shows that the system is indeed forming hierarchies of interpenetrating simple cubic lattices (Fig. 4.2). The density of each crystal state stays nearly constant throughout a range of μ , followed by a sudden jump at a threshold μ , making a higher density crystal. This near-constant density for each crystal suggests that there is only a very narrow range of density for each crystal to be thermodynamically stable. Crystal VI is the highest density crystal we obtained. High density crystals beyond crystal VI might exist, but as more cores of the particle reside in a lattice unit cell, the core-core repulsion may frustrate the formation of higher density crystals.

To map out the phase behavior of these crystals, we estimate an upper bound for the melting temperatures of each crystal. We anneal the crystal at a series of increasing T at fixed density until there is a discontinuous melting (Fig. 4.3). This likely overestimates the thermodynamic melting temperature. Using the estimated melting temperatures, we plot the phase diagram in Fig. 4.4. The shaded areas between the narrow stable regions are phase coexistence regions. The phase boundaries of other geometries are partially drawn in scale on the bottom left corner in the graph for comparison.

The melting temperatures increase as the system reaches higher density with more interpenetrating lattices, contrary to polyamorphous geometries which have lower T_c for transitions between phases with more interpenetrating networks, *i.e.* the T_c for each subsequent transition is always less than previous phase transitions (as a function of density) in all polyamorphic systems. This would be expected if the larger density crystals were able to form with fewer defects, and hence a *lower* energy per site. However, our

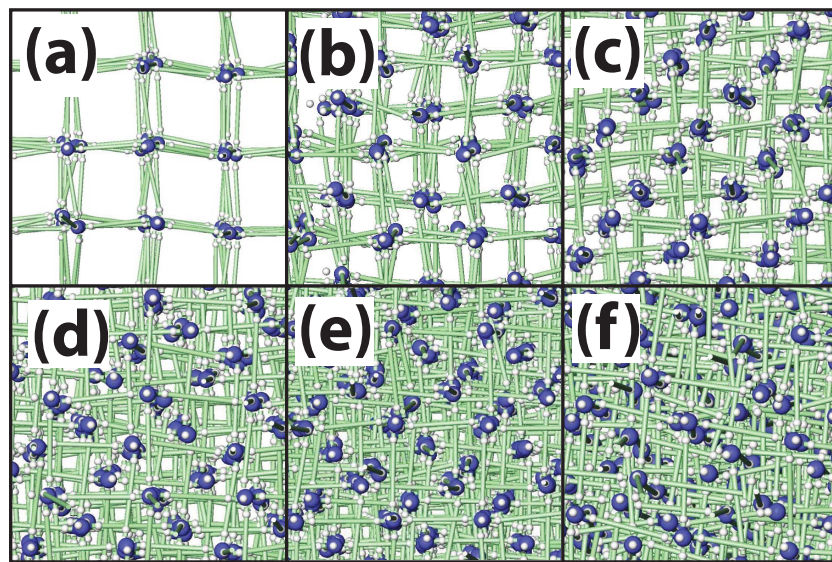


Figure 4.2: Visualization of the interpenetrating lattices of (a) crystal I ($T = 0.08311$, $\rho d^3 = 1.0$), (b) crystal II ($T = 0.08311$, $\rho d^3 = 2.0$), (c) crystal III ($T = 0.08311$, $\rho d^3 = 3.0$), (d) crystal IV ($T = 0.08311$, $\rho d^3 = 4.0$), (e) crystal V ($T = 0.08311$, $\rho d^3 = 5.0$), and (f) crystal VI ($T = 0.08310$, $\rho d^3 = 6.03$). Specifically, in (b), the core of a DNA complex locates roughly in the center of the other lattice unit cell, a result of two interpenetrating lattices. Due to the large amount of empty space, this motif can be repeated.

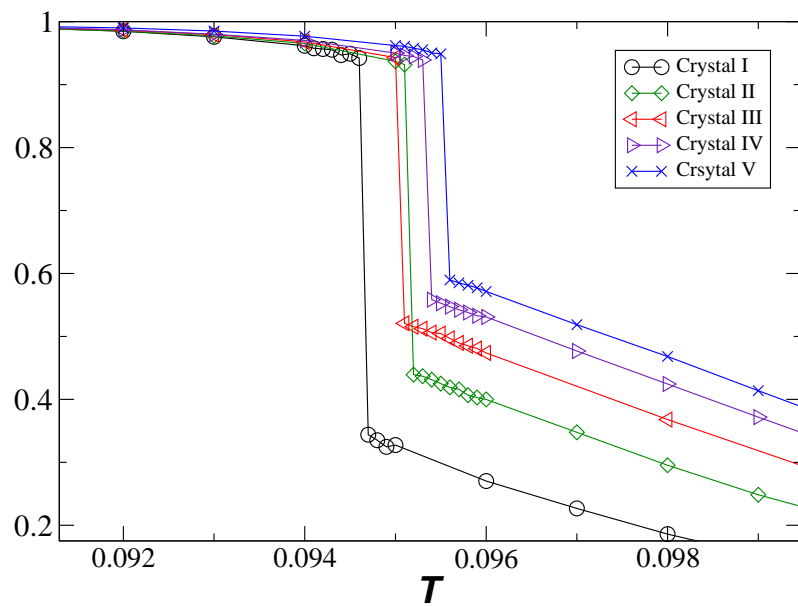


Figure 4.3: The percentage of intact bonds as a function of T on heating for crystal I–V. The discontinuity provide an upper limit on the melting temperature.

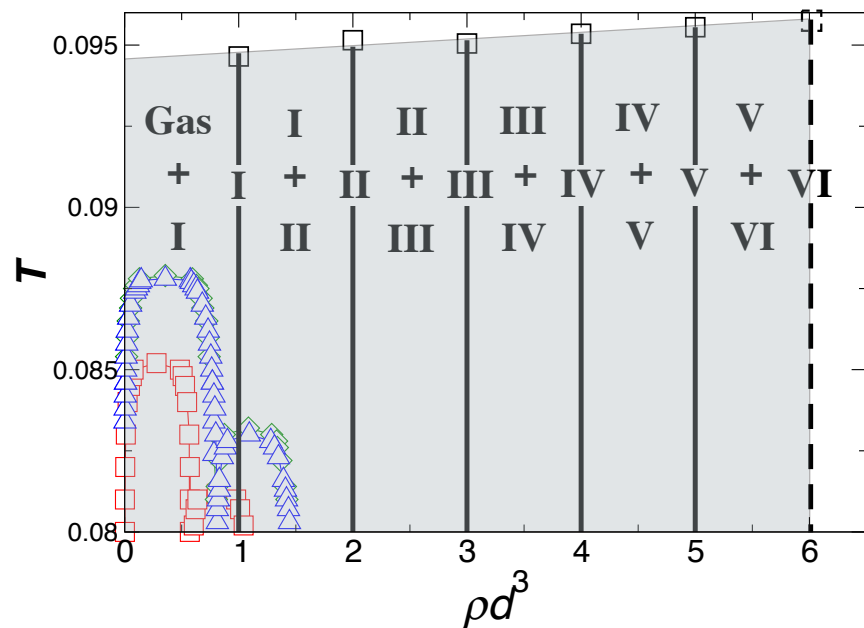


Figure 4.4: $T - \rho$ phase diagram of multiple crystals formed by octahedral nanoparticles. The density is scaled by d^3 . The gray regions indicate phase coexistence between crystals, except for the smallest density, where crystal I coexists with the gas phase. Crystal VI is observed but we are not able to obtain a reliable melting temperature, and therefore represented by the dashed lines. For comparison, we also show phase boundaries of the amorphous systems obtained in figure 3.1: red squares are for the tetrahedral orientation; blue triangles are for the 5-SBP; green diamonds are for the 5-TBP.

numerical data show that the energy per site for the larger density crystals is progressively *larger*, and hence less energetically stable (Fig. 4.5). Instead, we can understand the density dependence from the perspective of the Lindemann criterion [92], *i.e.* that a crystal typically melts when its vibrational amplitude reaches a critical fraction of the bond length. The repeated interpenetration of disconnected networks reduces the available space, and correspondingly decreases the vibrational amplitude, while the bond length remains unchanged. As a result, the larger density crystal will only melt at larger T . In contrast, for other polyamorphous geometries, there is no regular confinement of the “network sites,” and therefore the Lindemann criterion does not apply. Instead, the formation of the second interpenetrating network unavoidably distorts and destabilizes the first network, making both networks more susceptible to high temperature, thereby depressing T_c .

4.2 Structure

To quantify the crystal structure, we calculate the structure factor $S(q)$ (Fig. 4.6). The sharp peaks exhibited by all densities of crystals are indicators of ordered crystals, consistent with the interpenetration of well-defined crystal I in higher density crystals. Specifically, based on the visualization snapshots (Fig 4.2) and the fact that octahedral geometry tends to construct simple cubic lattice, we expect crystal I to be simple cubic lattice and crystal II to have DNA complex cores located near BCC lattice sites. This is confirmed by including the theoretical values for the peak positions for a simple cubic lattice for crystal I, and the theoretical values for peak positions of a BCC lattice for crystal II [93]. In the region $q \lesssim 2.8$, the peak locations of both crystal I and II match the predicted q values for SC and BCC lattice. Furthermore, the amplitude of $S(q)$ for crystal II is around twice that of crystal I at corresponding q values, in agreement with the theoretical prediction. There are peaks in $S(q)$ of crystal II at region $q \lesssim 2.8$ which are not predicted by the theoretical calculation. They occur at q values predicted for

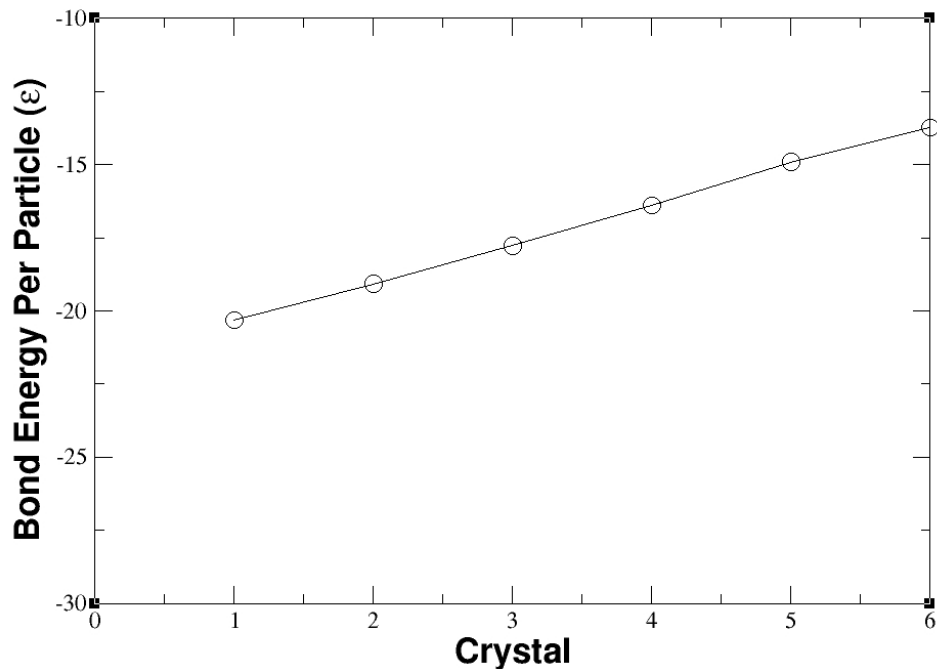


Figure 4.5: Bond energy per particle as a function of crystal hierarchy (crystal I–VI). The function is monotonic increasing, suggesting that the interparticle bonds become weaker as more interpenetrating lattices form. This is due to the crowding packing that distorts the bonds. For crystal I–V, $T = 0.08311$, crystal I ($\rho d^3 = 1.0$) has 125 NP, and crystal II ($\rho d^3 = 2.0$) has 250 NP, etc. For crystal VI ($\rho d^3 = 6.0$), $T = 0.08310$, and the system has ~ 1200 NP. This slight difference in tempeature and system size should have negligible effect on particle energy shown in the graph.

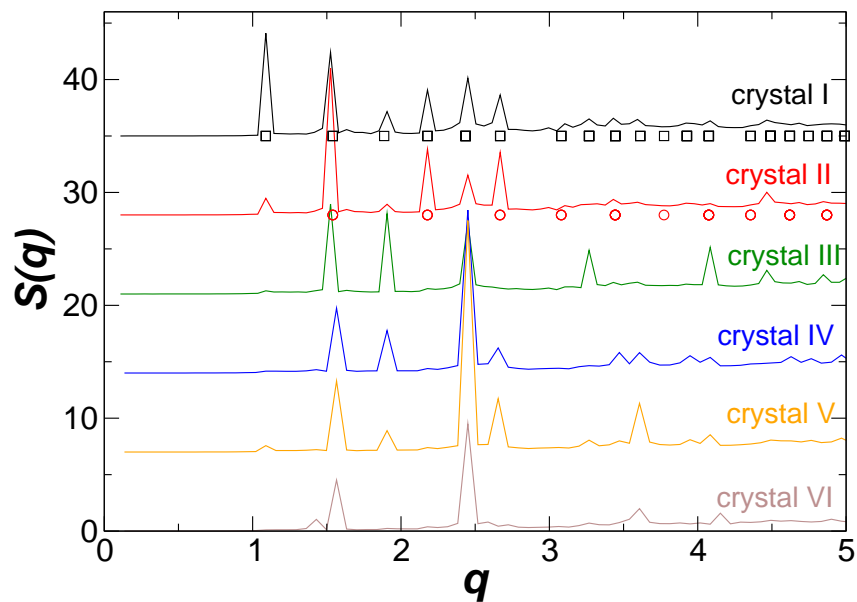


Figure 4.6: $S(q)$ for the hierachial crystal phases formed by octahedral geometry. For clarity, lines are shifted vertically so that each crystal is 7 units apart. The black squares below crystal I are the theoretically expected locations for the peaks of a perfect simple cubic lattice; similarly, the red circles below crystal II are the expected locations for the peaks of a perfect BCC lattice.

crystal I but have much smaller amplitude, suggesting that they are residual traits of crystal I, which did not die out completely due to the imperfections of crystal II.

4.3 Crystallization Dynamics

The conventional mechanism for crystallization follows the “two-step” pathway: the system first forms densified amorphous precursor before nucleating to an ordered structure. This scenario has been demonstrated in the crystallization of protein and colloids [63–72]. With our 6-functional NP system where novel polymorphs occur (section 4.1), we now examine this mechanism in a more unusual context. In particular, we compare three scenarios: (i) spinodal-aided (phase separation driven) crystallization, (ii) the self-assembly driven crystallization, and (iii) crystallization in polymorphous system. To select systems for these three scenarios, we resort to the close-up phase diagram for 6-functional units at the region of crystal I and II (Fig. 4.7). The white squares in the figure locate the melting temperatures for cryrstan I and II, and the solid lines denotes the thin regions where stable crystals form. The amorphous phase boundaries (the dotted lines) are estimated by extrapolating the phase boundaries of NP functionalized by 3, 4, or 5 DNA strands in Fig. 3.1.

Since at low temperature the bond lifetime increases, the the system dynamics might be kinetically hindered or significantly slowed down to an extent that the equilibrium is inaccessible to our computation time. Thus we focus on quenches to $T = 0.089$ where we empirically find the crystallization proceeds most readily. We investigate systems at $\rho d^3 = 0.5$ (Fig. 4.7 point A), $\rho d^3 = 1$ (point B), and $\rho d^3 = 1.5$ (point C). We keep volume V fixed, so these three densities correspond to $N = 500, 1000, 1500$, respectively. The system at $\rho d^3 = 0.5$ is located in the amorphous phase separation region, whereas other two systems at $\rho d^3 = 1$, and $\rho d^3 = 1.5$ are outside of any amorphous-amorphous phase transition. The system at $\rho d^3 = 1.5$ undergoes phase separation into crystal I and II, allowing us to examine the crystallization in polymorphous system.

Therefore, these three systems allow us to separately address the role of single versus double-interpenetrating crystals (point B and C), and spinodal-assisted versus assembly-driven crystallization processes (point A and B). Accordingly, we can determine if the mechanism of crystallization for interpenetrating networks differs from that for a single network, and compare difference between spinodal driven versus self-assembly driven clustering.

4.3.1 Cluster Size and Global Order Parameters

The conventional crystallization theory suggests that the crystallization is a two step process in which amorphous cluster proceeds the ordering process (section 1.4). To test the applicability of the mechanism, we need to separately identify the formation of dense clusters and the degree of crystallinity of those clusters. First, we evaluate the evolution of the cluster size directly from the number of bonded units and calculate the weighted mean cluster size $s(t)$, defined as,

$$s(t) \equiv \frac{\sum_{\text{clusters}} n^2 P(n)}{\sum_{\text{clusters}} n P(n)}, \quad (4.1)$$

where n is the size of a cluster at some time t . In this definition, larger clusters account more weight than smaller clusters due to the second moment n^2 in the formula. Intuitively, this definition gives the size of a randomly chosen cluster (in which larger cluster has higher probability to be chosen), as opposed to average size of all clusters, which is biased by numerous small clusters.

Following the approach in ref [94], we can identify crystal-like regions using an orientational order parameter Q_l , defined by a sum over spherical harmonic functions $Y_{l,m}(\hat{\mathbf{r}})$ using the unit vectors $\hat{\mathbf{r}}$ defined by the nearest neighbors. The nearest neighbors may be defined by distance or by bonds, which we will discuss in the following texts. Formally, we can construct the *global* orientational order parameter Q_l from the *local* orientational

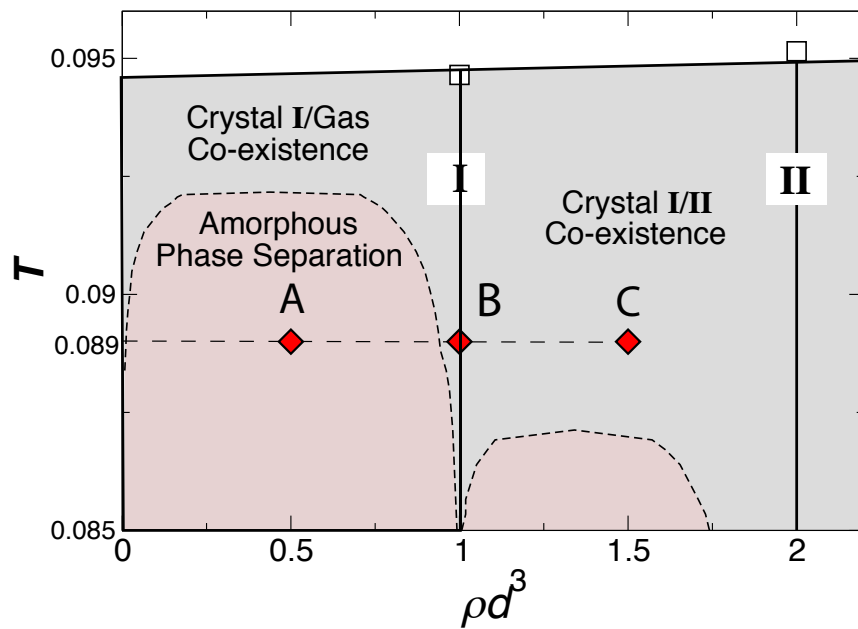


Figure 4.7: The close-up of phase diagram of the octahedrally functionalized NP at crystal I and II [75]. Solid vertical lines are the densities of crystal I and II; the crystals co-exist in the grey region between and melt on heating approaching the nearly horizontal line. The dotted lines are the estimated metastable amorphous phase boundaries for the “gas”-liquid ($0 < \rho d^3 < 1$) and liquid-liquid ($1 < \rho d^3 < 2$) amorphous phase transitions. The faded-red regions are the amorphous phase separation regions. The red diamonds indicate the state points where we quench to study the crystallization dynamics – point A in the phase amorphous separation region, and point B and C in assembly dominated regimes.

order parameter $\bar{q}_{l,m}(i)$, which is defined for each particle i in the system by

$$\bar{q}_{l,m}(i) \equiv \frac{1}{N_b(i)} \sum_{j=1}^{N_b(i)} Y_{l,m}(\hat{\mathbf{r}}_{ij}), \quad (4.2)$$

where $\hat{\mathbf{r}}_{ij}$ is the vector joining particle i and its neighbor j . The sum runs over all $N_b(i)$ bonds that particle i has with its neighbors. The spherical harmonics $Y_{l,m}(\hat{\mathbf{r}}_{ij}) = Y_{l,m}(\theta_{ij}, \phi_{ij})$ can be uniquely determined given a reference coordinate, and thus the local orientational order parameter $\bar{q}_{l,m}(i)$ is dependent on the chosen coordinate frame. We can average this local orientational order parameter over all N particles to obtain the *global* orientational order parameter $\bar{Q}_{l,m}$:

$$\bar{Q}_{l,m} \equiv \frac{\sum_{i=1}^N N_b(i) \bar{q}_{l,m}(i)}{\sum_{i=1}^N N_b(i)} \quad (4.3)$$

The $\bar{Q}_{l,m}$ still depends on the choice of reference frame. To remove this dependence, we construct rotationally invariant combinations,

$$Q_l \equiv \left[\frac{4\pi}{2l+1} \sum_{m=-l}^l |\bar{Q}_{l,m}|^2 \right]^{\frac{1}{2}} \quad (4.4)$$

Among the various choices for the degree l of $Y_{l,m}(\hat{\mathbf{r}})$, $l = 4$ provides the strongest signal for the expected cubic symmetry (the symmetry of lattices formed by octahedrally oriented valency); specifically, $Q_4 = 0.764$ for an ideal SC lattice. To capture the locally SC structure in case of two separate lattices, we use “bondedness” as the criterion for neighbor, namely, we consider only bonded neighbors when calculating Q_4 , excluding unbonded ones, which might have small separation but belong to distinctly bonded network. We compute Q_4 for all three systems $\rho d^3 = 0.5, 1, 1.5$. Additionally, we compute Q_6 , to identify potential body-center-cubic (BCC)-like structures. The theoretical value for a perfect BCC lattice is $Q_6^{\text{BCC}} = 0.511$. The Q_6 value in $\rho d^3 = 1.5$ system will capture the BCC-like structure of non-bonded units that might arise due

to interpenetration. We compare this value with the Q_6 of system at $\rho d^3 = 1$, where no interpenetration of lattices occurs. For the calculation of BCC order, we use spatial separation, rather than bonds, to determine neighbors, since the units comprising the BCC structure are actually unbonded first neighbors in the separate lattices. We note that for amorphous systems, $\bar{q}_{l,m}(i)$ adds up incoherently, so $\bar{Q}_{l,m} = 0$ and subsequently $Q_l = 0$ in the thermodynamic limit, so that one immediately distinguish crystal from amorphous systems.

4.3.2 Identification of Crystalline Clusters

While Q_4 and Q_6 are useful to identify global crystallinity in a given configuration, they are less helpful in identifying the presence of local crystal regions embedded in a larger amorphous cluster. Identification of these local regions is necessary to determine if crystallization and clustering occur simultaneously, or if amorphous clusters form first, and subsequently evolve crystalline order. Following ref [94], we identify crystal-like particles using a local invariant $q_4(i)$ for each individual particle, and the corresponding complex vector $\mathbf{q}_4(\mathbf{i})$. We use $q_4(i)$ instead of $q_6(i)$ because the local geometry for one particle has to be SC-like due to the octahedral symmetry. A particle is said to be crystal-like if it has a minimum number of neighbors with crystal-like connections. Bonded particles i and j are said to have a crystal-like connection if the vector dot product $\mathbf{q}_4(\mathbf{i}) \cdot \mathbf{q}_4(\mathbf{j})$ exceeds a threshold value. By comparing the distribution of dot product values of amorphous systems with well-crystallized systems (Fig. 4.8), we find that a threshold value $\mathbf{q}_4(\mathbf{i}) \cdot \mathbf{q}_4(\mathbf{j}) \geq 0.95$ for the dot product value (near the crossing point for the crystal and amorphous distributions) identifies $\approx 92.6\%$ of bonds in crystal state, and only misidentifies $\approx 1.3\%$ of the bonds of the amorphous system as crystal-like in system at $\rho d^3 = 0.5$. Similar precision is found in other two systems at $\rho d^3 = 1$ and $\rho d^3 = 1.5$. Finally, analysis of those same systems shows that we reliably define a crystal-particle if it has at least three crystal-like bonded neighbors (Fig. 4.9).

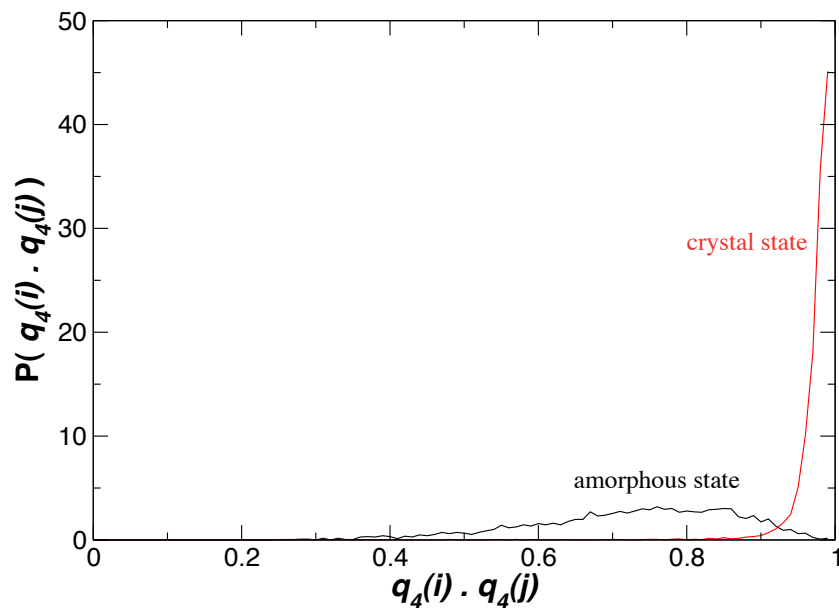


Figure 4.8: The distribution of the values of $\mathbf{q}_4(i) \cdot \mathbf{q}_4(j)$ for two systems at $\rho d^3 = 0.5$, $T = 0.089$, one crystallized and one in amorphous state. For crystallized systems, the values of the dot product narrowly peak at regions close to 1. For amorphous systems, the values have a wide distribution at $\mathbf{q}_4(i) \cdot \mathbf{q}_4(j) \approx 0.5 \sim 0.9$. Therefore using the threshold value $\mathbf{q}_4(i) \cdot \mathbf{q}_4(j) \geq 0.95$ (near the crossing point for the crystal and amorphous distributions), we identify most ($\approx 92.6\%$) crystal bonds, and only misidentify very little ($\approx 1.3\%$) amorphous bonds.

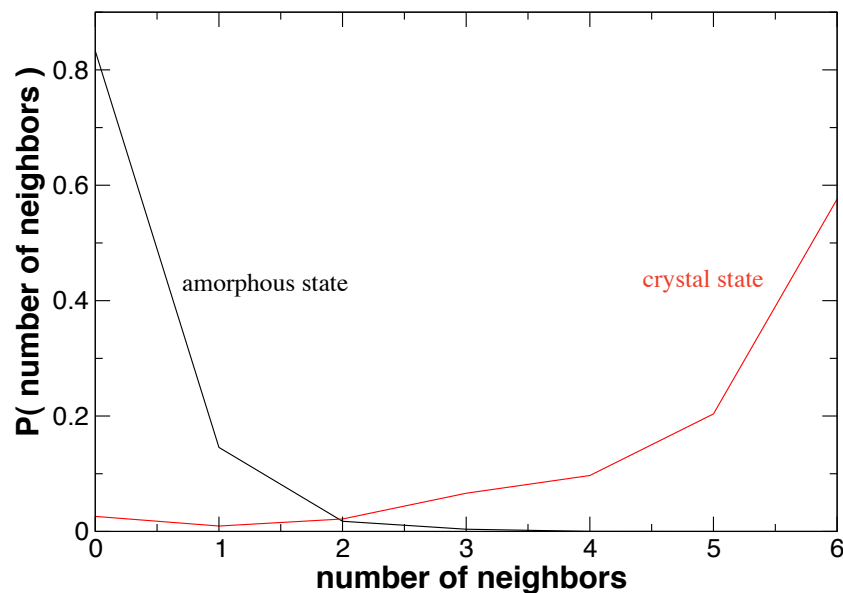


Figure 4.9: The distribution of the number of neighbors with “crystal-like connection” based on threshold value $\mathbf{q}_4(\mathbf{i}) \cdot \mathbf{q}_4(\mathbf{j}) \geq 0.95$ (see text) for two systems at $\rho d^3 = 0.5$, $T = 0.089$, one crystallized and one in amorphous state. Using the threshold value *crystal-like bonded neighbors=3*, we identify most ($\approx 94.3\%$) crystalline particles, and only misidentify very little ($\approx 0.4\%$) amorphous particles.

4.3.3 Time Evolution of Crystallization

We examine the evolution of the crystallizing systems by evaluating the fractional cluster size s/N , the (fractional) number of crystal-like particles N_x/N , and the normalized average orientation $Q_4/Q_4^{\text{cubic lattice}}$, so that all quantities vary over the range $[0, 1]$ (Fig. 4.10).

We find that all systems undergo a condensation from an unbonded disordered state to a dense large amorphous cluster within $t \approx 10$ Monte Carlo Steps (MCS). Both Q_4 and N_x remain small for $t \lesssim 10^4$, demonstrating the amorphous nature of the cluster. The ordering process only occurs much later, at $t \approx 10^4$ when Q_4 and N_x rise sharply within a narrow window of time. The time needed for crystallization is strongly T dependent, and at low T the amorphous cluster can persist for times scales longer than we can simulate. Fig. 4.11 shows the time needed to produce 50 crystalline NP at $T = 0.082 \rightarrow 0.090$. Above $T \approx 0.091$, the system does not crystallize. Since the ordering happens over a relatively narrow time window, the global Q_4 is itself an indication of crystal formation. The fraction N_x/N never reaches one, since there are always surface particles of the crystal that will not be identified as crystal-like.

For the highest density $\rho d^3 = 1.5$, we wish to further determine if the formation of a double network occurs simultaneous with, or after the formation of a single SC network. To test this, we check for the presence of BCC order in the lattice using Q_6 and compare its evolution relative to Q_4 . For reference, we first consider $\rho d^3 = 1.0$ where there should be no interpenetration, so that we know to what degree Q_6 might give a false signal of interpenetration. Fig 4.10(b) shows that $Q_6/Q_6^{\text{BCC}} \approx 0.6$ for the final SC crystal, consistent with the theoretically expected value $Q_6^{\text{SC}}/Q_6^{\text{BCC}} \approx 0.6 = 0.693$. Fig. 4.10(c) shows that the growth of Q_6 for the high density system tracks the temporal behavior of Q_4 . Thus, that the formation of an interpenetrating structure appears to occur at the same time as SC ordering. Note that the asymptotic value of N_x/N in Fig. 4.10 for $\rho d^3 = 1$ and 1.5 ($N_x/N \approx 0.95$) is slightly larger than for $\rho d^3 = 0.5$ ($N_x/N \approx 0.81$).

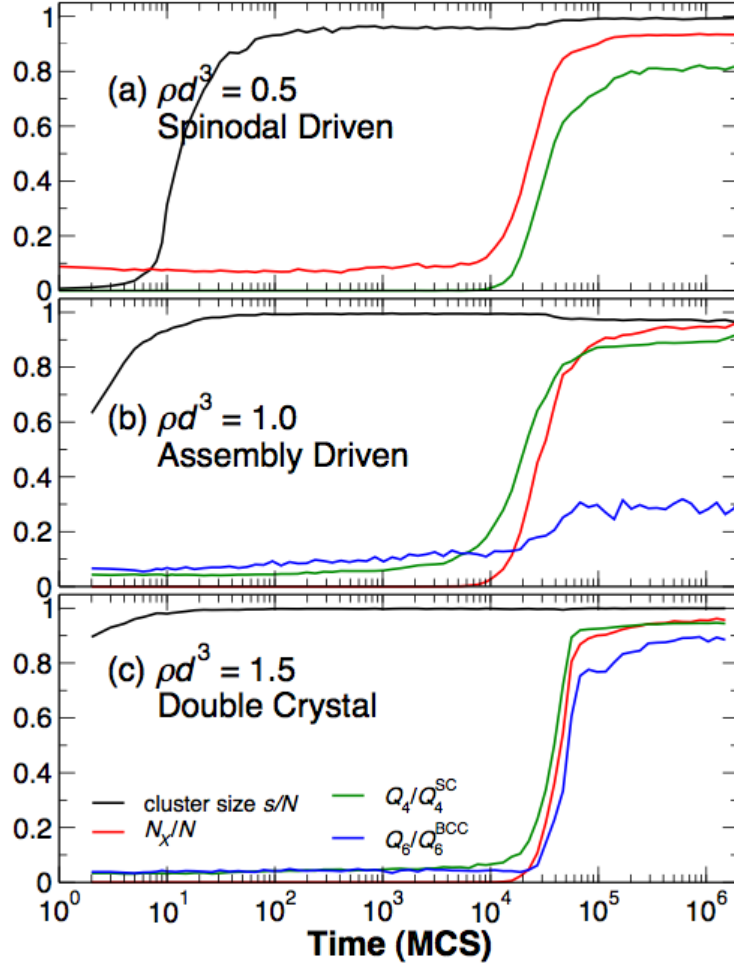


Figure 4.10: The time evolution of the clustering and crystallization process at (A) $\rho d^3 = 0.5$, where spinodal decomposition promotes clustering; (B) $\rho d^3 = 1$, the density of the single SC crystal, where self-assembly drives clustering; (C) $\rho d^3 = 1.5$ where there is a phase separation of the single and double interpenetrating crystals. For each density, we show the fractional cluster size s/N , the fraction of crystal-like particles N_x/N , and the normalized average orientation Q_4/Q_4^{SC} . For $\rho d^3 = 1$ and 1.5, we also show Q_6/Q_6^{BCC} to determine whether the formation of two interpenetrating crystals are simultaneous or occurs step-wise. The time is in Monte Carlo steps, defined in section 2.4. To improve the statistics of our results, we average over 5-15 independent runs for each crystallization system.

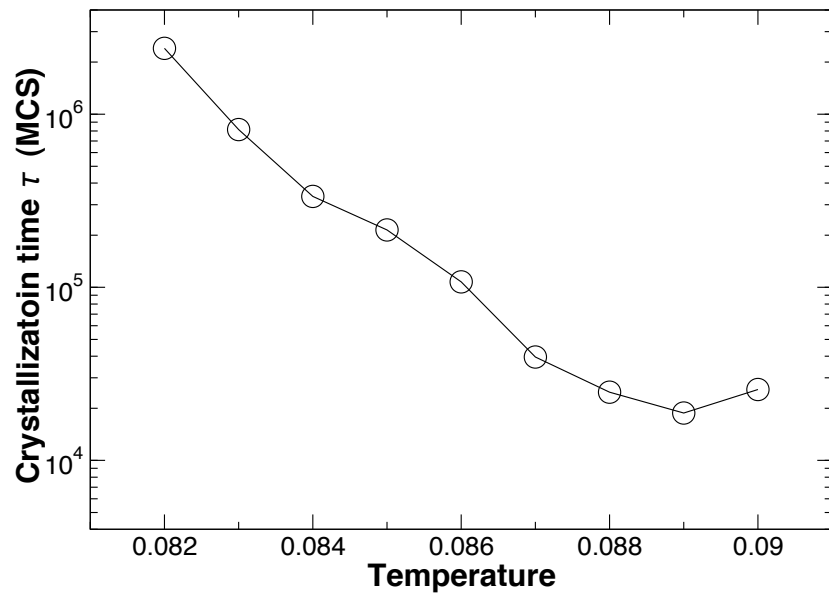


Figure 4.11: The crystallization time τ (in MCS) for the 6-functional NP system at $\rho d^3 = 0.5$. The crystallization time τ is the time (MCS) required to generate 50 crystal particles as a function of temperature T . We note that once the system reach 50 particles, it always crystallizes fully except a small number of surface NP. Because the nucleation process happens rapidly (Fig. 4.10), the time needed to reach 50 crystalline NP is a good measurement of the crystallization time.

This is because we use a larger N , and thus the surface-to-volume ratio is smaller, and so the effect on N_x/N is smaller.

For both densities, note that s slightly increases upon crystallization. Presumably the long ranged order allows for the formation of some additional bonds that were dangling in the clustered, but disordered state. For $\rho d^3 = 1.5$, s has a very small but noticeable *decrease* immediately prior to ordering. This can be understood by the fact that the formation of two interpenetrating SC lattices requires a separation of two lattices; therefore, there must be a temporary breaking of amorphous bonds between locally cubic lattices before ordering, temporarily decrease s .

The observed sequence of densification followed by ordering for *all* densities confirms that the crystallization dynamics for the DNA-linked NP follows a conventional “two-step” pathway of crystallization – even in the case where a double-interpenetrating network must form. Depending on density, the dense intermediate is driven either through metastable phase separation or self-assembly. Thus, the same framework used to understand protein and colloid crystallization kinetics also applies to this more unusual material. For these relatively high concentrations, the clustering can happen rapidly, and therefore the ordering step is the rate determining one.

We directly visualize the crystallization of two systems ($\rho d^3 = 0.5$ and $\rho d^3 = 1.5$) at three important points: (i) clustering prior to ordering; (ii) the ordering process, and (iii) after ordering (Fig. 4.12). The identified crystal-like NP are colored in red with a slightly larger radius. From Fig. 4.12 (b) and (e) we can clearly see the interface between crystal and amorphous phases. Fig. 4.12 (b) has two separate SC lattices, an evidence of multiple nucleation cores.

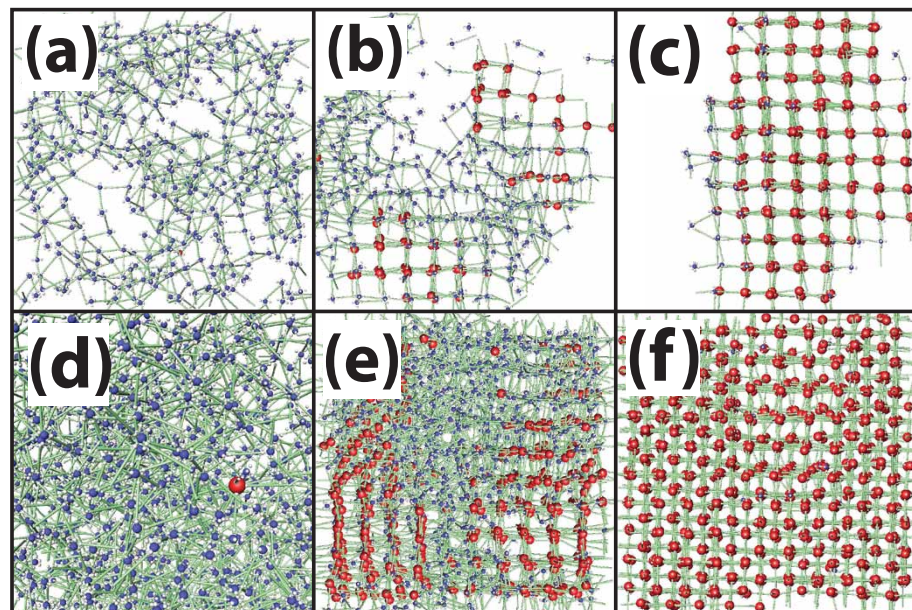


Figure 4.12: Visualization of the system at three points during crystallization. (a)–(c) are at density $\rho d^3 = 0.5$. Specifically, (a) is system after clustering but prior to ordering; (b) is during the ordering; (c) is after ordering. (d)–(f) represent the same time progression but at density $\rho d^3 = 1.5$. The identified crystal-like particles are colored in red with a slightly larger size in representation.

Chapter 5

Discussion

In this chapter we discuss our results in the context of other theoretical and experimental works. Section 5.1 identifies the common theme of interpenetration in amorphous and crystal systems; section 5.2 explores the implications of the two-step pathway mechanism with reference to recent experimental studies.

5.1 Interpenetration of Networks and Lattices

We have demonstrated that DNA-functionalized nanoparticles with several different numbers of DNA-arms and different directionalities exhibit a rich phase behavior: the tetrahedral geometry forms four amorphous phases accompanied by three first order critical points (from ref. [19]); the 5-SBP and 5-TBP (Fig. 2.4) have three amorphous phases accompanied by two critical points; the octahedral geometry makes at least six polymorphous crystals. The common motif for all geometries is the repetition of networks that utilize the empty spaces in other networks and thereby interpenetrate each other. Indeed, such interpenetrating lattices occur in nature in crystal forms, such as in ice VI, VII, and VIII [95]. This interpenetration likely also plays a secondary role in the hypothesized liquid-liquid transition of water [48, 49]. We expect that the in-

terpenetration of networks is more limited in traditional molecular systems than our DNA-functionalized nanoparticles, since, unlike the DNA system, the range of attraction between traditional molecules is only slightly larger than the core repulsion size. Such short bond distances (as compared to the repulsive core size) provide limited empty space and significant hard-core interactions frustrate the formation of additional interpenetrating networks. Conversely, for longer ssDNA (provided the length is shorter than the persistence length), even further repetition of the interpenetration process may be possible [58].

In our system we find the phase coexistence region shrinks as the valency γ decreases, in agreement with previous studies [44, 87] (Fig. 5.1). As a result, the limited valency opens a large region of densities that can be occupied by the complementary networks. Furthermore, the phase coexistence regions for the second phase transition also shrink at decreasing γ (Fig. 3.1), opening the possibility for a third interpenetrating network. To our knowledge, it is the first time the phase boundaries of liquid-liquid transition are examined with respect to valency. The emergence of thermodynamically distinct phases at higher density appears to rely on the specific directionality of bonding interactions. Indeed, systems with only limited valency do not show additional phase transitions [44, 83, 87, 88]. The directionality is further enhanced by the lock-and-key mechanism of DNA that ensures one bond per bonding site, as opposed to systems where multiple bonding sites may form simultaneous pairs of bonds. Such simultaneous bonding would lead to (i) a more crowded local environment with associated distortion of the network and absence of the empty space and (ii) the possibility of additional interactions between distinct networks. Indeed, the lock-and-key interaction is a fundamental ingredient since it is responsible of the inertness of the networks which condensate from the phase separation process. Without the lock-and-key specification, the phase behaviors would be much more irregular. We demonstrate this point by comparing the phase diagram of our 6-patchy NP (Fig. 4.4) with that of the 6-functional NP model by Doye *et al.* (Fig. 5.2(a)), both with octahedral symmetry. We see that the patchy particles, which

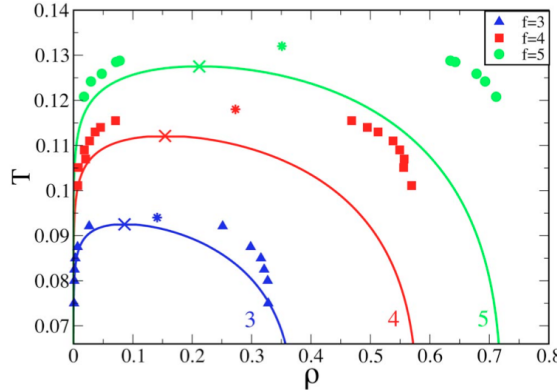


Figure 5.1: Gas-liquid phase transition boundary in $T-\rho$ plane from ref. [44]. From both simulation (dots) and theory (solid lines), Sciortinos and co-workers found that gas-liquid coexistence regions shrink as functional patches decrease from $f = 5$ to $f = 3$.

do not have lock-and-key ingredient, form a variety of crystal structures in Fig. 5.2(b). We point out that the inertness of networks in our systems can potentially give better control in producing the desired structure, as the system makes only one type of crystal for a given density.

To put our simulation work in experimental contexts, we note that DNA strands have a weak electrostatic repulsion. It has been argued that weak repulsion between bonding strands would favor more ordered structures and reduce the probability of self-assembling into an undesirable structures [13]. This should reduce distortions of the network, thereby facilitating the interpenetration process. Additionally, due to the helical pitch of ≈ 10 base-pairs of DNA (Fig. 5.3), it may be experimentally important to consider using multiples of 10 bases to avoid stress that might distort the regularity of the structure.

The regularity of the tetrahedral and octahedral systems facilitates interpenetration. For the 5-SBP system, there is no possible regular space-filling network, and thus the distortion obstructs the formation of other complementary networks. Nonetheless, the system can still undergo two amorphous phase transitions and construct two interpen-

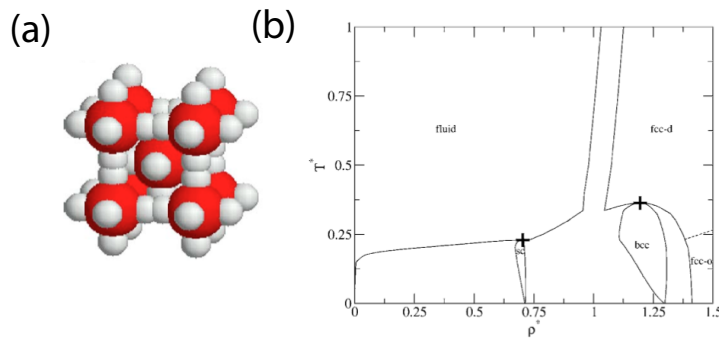


Figure 5.2: The model (a) and phase diagram (b) of the 6-functional patchy particles in ref [91]. The 6-patchy NP model is similar to our 6-functionalized NP, but without the lock-and-key requirement. The phase diagram therefore shows a variety of crystal structures that contrast the regularity of the crystal phases in our 6-functionalized NP in Fig. 4.4.

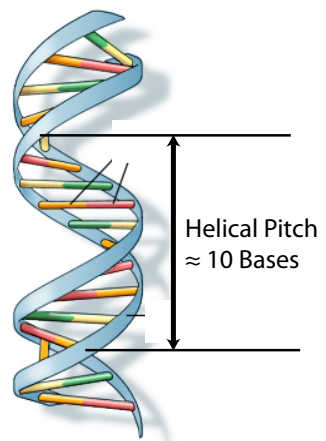


Figure 5.3: Double strand DNA helix. The helical pitch occurs every ≈ 10 bases.

etrating networks due to the ample empty space. The system can potentially form a third network, but unlike the tetrahedral system, we did not observe a clear phase separation in the corresponded high density region. In principle, the 5-TBP system could form connected hexagonal sheets, although we never observed such an ordered state. While this structure could tile space, it does not promote interpenetration, since the voids of such a network are dissimilar from the original network. As a result, we observe behavior nearly identical to that of the 5-SBP system. For the octahedral system, a well-defined ordered lattice allows the interpenetration of networks to occur more easily. We observed 6 interpenetrating simple cubic lattices, compared with only 3 and 2 networks are found in the amorphous 4-armed and 5-armed systems, respectively.

5.2 Crystallization Process

For the 6-functional NP, we have shown that all crystallizing systems follow the two-step mechanism in three investigated scenarios: (i) spinodal-assisted (phase separation driven) crystallizing to single SC lattice; (ii) self-assembly driven formation of dense liquid crystallizing to single SC lattice; (iii) self-assembly driven formation of dense liquid crystallizing to coexistence of single and double SC lattices. While assembly-guided crystallization has previously been documented in colloidal and protein system [64, 73], this is the first time the two-step crystallization pathway is observed in polymorphous materials, giving strong evidence to the universal nature of the mechanism.

Between the two driving mechanism for crystallizatoin, we point out that the phase separation in our system is much weaker than assembly driving force, evidenced in the system at $\rho d^3 = 0.5$ crystallizing inside the metastable gas-liquid region but still follows almost identical evolution trajectory as systems without phase separation. Such a pronounced self-assembling feature in our model is due to the highly specified DNA orientation and the cooperative bonding that together assist the local densification and crystal symmetry development.

With respect to the geometry, the regular space filling geometry of the units clearly aids the process. However, it is not a sufficient condition for crystallization, as crystal structure was never observed in the tetrahedral amorphous networks constituted of NP of the same model but with four ssDNA in tetrahedral coordination [19], even though tetrahedral is a regular space-filling geometry.

5.2.1 Comparison with Experiments

It is important that we compare our results with the recent experimental studies of Mirkin and co-workers [31], where they report a 3-stage crystallization process for uniformly DNA-coated NP (Fig. 5.4). The study found that the NP initially form small amorphous aggregates, and these clusters separately evolve crystallinity at stage two. The ordered but dispersed clusters eventually coalesce into a large final crystal lattice. As noted by these authors, this last stage of crystallization is probably driven by Ostwald ripening, a mechanism that is relatively well explored. Accordingly, these experiments also fit within the general framework of the two-step process: the small amorphous aggregates in phase 1 is the first step in the two-step mechanism convention; these small amorphous clusters then nucleate into discrete crystal domains in phase 2, which is characteristically the second step.

The difference between this experimental system and our simulation is that the crystal growth in the experimental system is rather slow, stretching from phase 2 to phase 3. Since our simulations shown do not exhibit this very slow growth of the crystal, we also check where such slow ripening might occur under different thermodynamic conditions. Indeed, simulations at lower density ($\rho d^3 = 0.3$) evolves crystallinity in small region within the amorphous cluster. The subsequent growth of this crystal is so slow, that we are not able to complete the crystallization in the computational time frame of the simulation. This observation demonstrates that the second step (in the two-step mechanism convention) in the process can vary significantly depending on the state

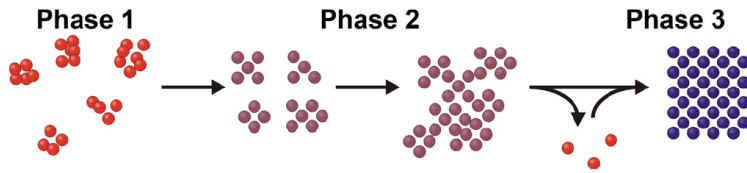


Figure 5.4: The schematic of the three-step crystallization pathway proposed in ref. [31]. At phase 1 the DNA-functionalized NP form small amorphous clusters. These small amorphous clusters separately evolve crystallinity in phase 2 before they coalesce into a large crystal at phase 3, during which the different discrete crystalline domains reorient to develop a global crystallinity.

point chosen. In our case, the chosen density (or concentration) plays an important role in the nucleation rate. In the experiment by Mirkin and co-workers [31], the nucleation rate is largely dependent on the characteristics of interparticle interactions, such as the DNA bond length and strength and the type of system (binary or homogeneous NP). These considerations are discussed in the thesis of Olivia Padovan.

We should note a potentially important difference between our simulations and that of the experiments in ref. [31]. For the uniformly coated NP used experimentally, the local NP binding is not predisposed to reflect the order of the eventual crystal state. In contrast, our 6-armed units bind in such a way that readily reflects SC symmetry. The coarsening to the eventual crystal state should occur more readily in the case where the crystal order is reflected in the symmetry of local bonding. Regardless, the similarity of all our simulated systems and other experimental systems leads us to conclude that a two-step approach is an apparently universal phenomenon.

Our model also points to a direction for future research. Since there are no NP attractions in our model (other than DNA linking), the gas-liquid phase separation is driven by the self-assembling DNA-hybridization. If, in addition to the hybridization, there were isotropic NP attractions, the system might be able to form a much higher density droplet controlled by the packing of the NP cores (Fig. 5.5). This could result in a

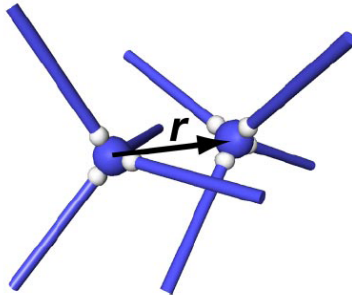


Figure 5.5: If two DNA-functionalized NP are not aligned along their ssDNA arms, it is possible that two NP bonds via isotropic attractive core-core interaction at a close distance r . In this case the amorphous state may be much *denser* than the final crystal structure, which is scaffolded by dsDNA links. We point out that in our system we do not have such attractive potential between nano-cores. Picture courtesy to ref. [19].

crystallization by hybridization that would actually dramatically *decrease* the density relative to the amorphous cluster, since the formation of dsDNA links will open the structure. Such an intermediate not created by DNA base-pairing might offer different pathways to create crystals, avoiding the kinetic traps that are encountered experimentally. We are not aware of any experimental work that has utilized this idea.

5.2.2 Why is Crystallization Hard?

Before answering the question, we need to understand “why is the two-step process universal across all crystallization systems?” To start with, our results show that the transition from an amorphous state to an ordered, crystalline state requires at least a highly ordered group of particles to serve as a nucleation core. Although the directional bonding combined with high cooperativity of the dsDNA bond already locally encodes the long-ranged structure of the crystal, this cannot serve as substitute for an amorphous precursor to the crystal state. Such an universal amorphous precursor can be explained by the multiplicities of the amorphous states. When a system condenses, either through self-assembling or phase separation, the system inevitably enters the amorphous state

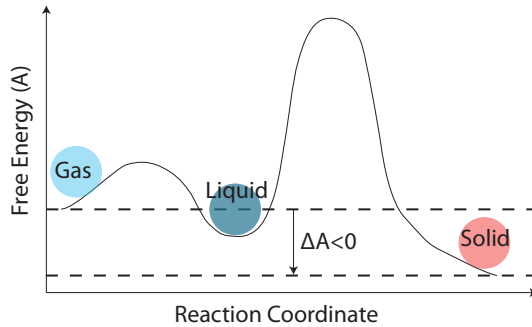


Figure 5.6: The schematic of the free energy pathway of crystallization. For the canonical ensemble in our system, Helmholtz free energy (A) is used, although similar pathway is expected for other ensembles. The final crystal state has lower free energy and thus is thermodynamically more favorable. However, the kinetic barrier between amorphous liquid and crystal state is substantially higher than the barrier between gas and liquid, and thus nucleation step is much slower than the densification.

due to its overwhelming multiplicities compared with that of the thermodynamically more stable crystal phases. After a long evolution, a critical number of ordered NP then “realize” that the crystal phase has lower free energy, which initiates the second step: nucleation. This “realization” is, in general, difficult, as shown in the schematic of free energy pathway in Fig 5.6. In the graph, we show that the free energy barrier between liquid state and the crystal state is substantially higher than the barrier between gas and liquid. We can understand this from the multi-dimentional structural space the liquid has to probe in order to construct crystals [73]. Intuitively, the transition from gas to liquid phase is a 1-dimensional density space, *i.e.* the system evolves along different densities. However, the liquid state has to explore a wide range of possible structures (a multi-dimentional space) before discovering the “correct” crystal structure. This process entails a much higher kinetic barrier and thus the nucleation is a rate-determining step in the reaction.

We can now try to answer the question why crystallization in self-assembly systems is difficult. In fact, even though many experimental systems of DNA-functionalized NP

were expected to form crystalline structure [85, 96], supported with theoretical predictions [14], the success did not come until very recently [27, 29]. The main reason is that, regardless of the system characteristics, the nucleation of NP is invariably preceeded by an amorphous state in which the system is often arrested by kinetics (in a gel-like state) and thus unable to evolve the thermodynamically favored crystalline structure. One factor that can cause this “trapped state” is the cooling temperature. Fig. 4.11 demonstrates that the crystallization time τ increases exponentially as the temperature deviates further from the optimal range, which is a narrow window of “crystallization slot”. This range is $T \approx 0.087\text{--}0.090$, corresponding to $\approx 28\text{--}38.5^\circ\text{C}$ [80, 97]. We emphasize that the ssDNA in our system is only 4 bases long; for longer ssDNA hybridization the crystallization will be significantly slowed down due to slowdown of hybridization and dehybridization process, and therefore the crystallization temperature slot would be much narrower than that in our simulation system [31]. Accordingly, the temperature can potentially prohibit the crystallization. Other factors such as DNA linker length and concentration would also play important roles in the dynamics. As all crystallizing systems inevitably enter the densified amorphous precursor, the real challenge of crystallizing NP systems lies in a careful control of various parameters in order to stay within the crystallization slot and overcome the kinetic barriers [66, 67, 73, 74].

Chapter 6

Conclusion

We have demonstrated that DNA-functionalized NP with specified number and directionalities of ssDNA tethers can self-assemble into polyamorphous and polymorphous structures. Specifically, the 3-TP NP has one amorphous phase transition, analogous to traditional materials; the 4-fucntional tetrahedral DNA dendrimers develop a rich phase behavior with 4 armophous states and 3 first order phase transitions [19]; the two 5-functional NP, 5-SBP and 5-TBP, make quantitatively similar phase boundaries that include three amorphous phases accompanied by two phase transitions. This multitude of amorphous liquid phases in the systems of 4-functional and 5-functional NP is unambiguously polyamorphism, a phenomenon experimentally found in phosphorus [47] and also suspected in other molecular systems such as water [48–53] and silica [55, 56]. We have also demonstrated that the discovered polyamorphism in our systems is a result of network interpenetration, with each higher density liquid consisted of one additional network. In particular, the emergence of polyamorphism in one of the 5-functional NP shows that interpenetration of networks does not require a space-filling geometry in the nano-building block. Lastly, the 6-functional octahedral units construct up to 6 interpenetrating simple cubic lattices through the same route of lattice interpenetration.

The crystallization dynamics of 6-functional octahedral units follows the conventional “two-step” pathway mechanism in which the system first forms densified liquid, followed by ordering within this amorphous cluster. We find that all three investigated scenarios follow this trajectory: (i) system crystallizing to single SC lattice driven by gas-liquid phase transition, (ii) systems crystallizing to single SC lattice driven by self-assembly, in the absence of amorphous phase transition, and (iii) systems crystallizing to coexisting single and double SC lattices driven by self-assembly, also in the absence of amorphous phase separation. These three scenarios demonstrate that, despite a strongly specified geometry in the building block NP, both spinodal-assisted and self-assembly driven crystallization requires an amorphous precursor. Furthermore, polymorphous structures do not change this reaction path. These findings concern the difficulties in crystallization and has important implications for the developments of nano-crystals.

The plethora of amorphous and crystal structures in DNA-functionalized NP holds great promise for future applications. The formation of low density NP assemblies with crystalline order is expected to be an important step toward the development of new materials with unusual optical or electronic properties [12, 14, 98]. Moreover, the possibility of multiple distinct networks may be developed into a new class of materials. For example, increasing the number of interpenetrating networks changes the lattice spacing and thus the scattering properties. Alternatively, distinct networks might serve as separate, but interwoven charge transfer conduits for electronic materials, as dsDNA and gold NP have conductivity comparable to semi-conductor [99–101]. From the crystallization dynamic analysis, we have shown that the highly specified DNA orientation in our model clearly helps building self-assembled higher order crystal structures. Future applications of such directionally controlled crystallizing building blocks include tethering nano-arms (*e.g.* ssDNA) to the active contact “patches” on protein surface to facilitate the currently challenging crystallography of protein [102], aiding pharmaceutical discovery. Using the enhanced assembly-driven crystallization provided by DNA bonding, it is possible to approach crystal-derived applications from a new perspective.

Bibliography

- [1] Crommie MF, Lutz CP, Eigler DM (1993) Confinement of electrons to quantum corrals on a metal surface. *Science* 262:218–220.
- [2] Ozin GA, et al. (2009) Nanofabrication by self-assembly. *Materials Today* 12:12–23.
- [3] Glotzer SC, Solomon MJ, Kotov NA (2004) Self-assembly: From nanoscale to microscale colloids. *AICHE Journal* 50:2978 – 2985.
- [4] Berti D (2006) Self assembly of biologically inspired amphiphiles. *Current Opinion in Colloid and Interface Science* 11:74 – 78.
- [5] Robinson BH, Seeman NC (1987) The design of a biochip: a self-assembling molecular-scale memory device. *Protein Engineering* 1:295–300.
- [6] Seeman NC (2003) Dna in a material world. *Nature* 421:427–430.
- [7] Beijer FH, Kooijman H, Spek AL, Sijbesma RP, Meijer EW (1998) Self-complementarity achieved through quadruple hydrogen bonding. *Ang. Chem.* 37:75 – 78.
- [8] Friedman RS, McAlpine MC, Ricketts DS, Ham D, Lieber CM (2005) Nanotechnology high-speed integrated nanowire circuits. *Nature* 434:1085.
- [9] ALIVISATOS AP, et al. (1996) Organization of 'nanocrystal molecules' using dna. *Nature* 382:609 – 611.

- [10] Chan G.; Mooney DJ (2008) New materials for tissue engineering: towards greater control over the biological response. *Trends in Biotechnology* 26:382–92.
- [11] Whitesides GM, Wong AP (2006) The intersection of biology and materials science. *A. P. MRS Bull* 31:19–27.
- [12] Crocker JC (2008) Nanomaterials: Golden handshake. *Nature* 451:528.
- [13] Licata NA, Tkachenko AV (2006) Statistical mechanics of dna-mediated colloidal aggregation. *Phys. Rev. E* 74:041408.
- [14] Tkachenko AV (2002) Morphological diversity of dna-colloidal self-assembly. *Phys. Rev. Lett.* 89:148303.
- [15] Hsu CW, Sciortino F, Starr F (2010) Theoretical description of the self-assembly dynamics of dna-functionalized nanoparticles. *preprint*.
- [16] Lukatsky DB, Frenkel D (2004) Phase behavior and selectivity of dna-linked nanoparticle assemblies. *Phys. Rev. Lett.* 92:068302.
- [17] Starr FW, Sciortino F (2006) Model for assembly and gelation of four-armed dna dendrimers. *J. Phys. Condens. Matter* 18:L347–L353.
- [18] Largo J, Starr FW, Sciortino F (2007) Self-assembling dna dendrimers: A numerical study. *Langmuir* 23:5896.
- [19] Hsu CW, Largo J, Sciortino F, Starr FW (2008) Hierarchies of networked phases induced by multiple liquid–liquid critical points. *Proc. Natl. Acad. Sci. U.S.A.* 105:13711–13715.
- [20] Winfree E, Liu F, Wenzler L, Seeman N (1998) Design and self-assembly of two-dimensional dna crystals. *Nature* 394:539.
- [21] He Y, et al. (2008) Hierarchical self-assembly of dna into symmetric supramolecular polyhedra. *Nature* 452:198–201.

- [22] Endo M, Majima T (2006) Thermodynamic properties of branched dna complexes with full-matched and mismatched dna strands. *Chem. Commun.* 22:2329–2331.
- [23] Mirkin CA, Letsinger RL, C. MR, Storhoff JJ (1996) A dna-based method for rationally assembling nanoparticles into macroscopic materials. *Nature* 382:607–609.
- [24] Glotzer SC, Solomon MC (2007) Anisotropy of building blocks and their assembly into complex structures. *Nature Materials* 6:557–562.
- [25] Condon A (2006) Designed dna molecules: principles and applications of molecular nanotechnology. *Nat Rev Genet* 7:565–75.
- [26] Valignat MP, Theodoly O, Croker JC, Russel WB, Chaikin PM (2005) Reversible self-assembly and direct assembly of dna-linked micrometer-sized colloids. *Proc. Natl. Acad. Sci. U.S.A.* 102:4225–4229.
- [27] Biancaniello PL, Kim AJ, Crocker JC (2005) Colloidal interactions and self-assembly using dna hybridization. *Phys. Rev. Lett.* 94:058302.
- [28] Kim AJ, Scarlett R, Biancaniello PL, Sinno T, Crocker JC (2009) Probing interfacial equilibration in microsphere crystals formed by dna-directed assembly. *Nat Mater* 8:52–55.
- [29] Kim AJ, Biancaniello PL, Crocker JC (2006) Engineering dna-mediated colloidal crystallization. *Langmuir* 22:1991–2001.
- [30] Park SY, et al. (2008) Dna-programmable nanoparticle crystallization. *Nature* 451:553–6.
- [31] Macfarlane RJ, et al. (2009) Assembly and organization processes in dna-directed colloidal crystallization. *PNAS* 106:10493–10498.
- [32] Schmatko T, et al. (2007) A finite-cluster phase in (lambda)-dna-coated colloids. *Soft Matter* 3:703–706.

- [33] Geerts N, Schmatko T, Eiser E (2008) Clustering versus percolation in the assembly of colloids coated with long dna. *Langmuir* 24:5118–5123.
- [34] Harris NC, Kiang CH (2005) Disorder in dna-linked gold nanoparticle assemblies. *Phys. Rev. Lett.* 95:046101.
- [35] Park SJ, Lazarides AA, Storhoff JJ, Pesce L, Mirkin CA (2004) The structural characterization of oligonucleotide-modified gold nanoparticle networks formed by dna hybridization. *J. Chem. Phys.* 108:12375.
- [36] Nykypanchuk D, Maye MM, van der Lelie D, Gang O (2008) Dna-guided crystallization of colloidal nanoparticles. *Nature* 451:549–52.
- [37] Xiong H, van der Lelie D, Gang O (2009) Phase behavior of nanoparticles assembled by dna linkers. *Phys. Rev. Lett.* 102:015504.
- [38] Endo M, Seeman N, Majima T (2005) Dna tube structures controlled by a four-way-branched dna connector. *Ang. Chem.* 44:6074–6077.
- [39] Endo M, Shiroyama T, Fujitsuka M, Majima T (2005) Four-way-branched dnaphyrin conjugates for construction of four double-helix-dna assembled structures. *J. Org. Chem.* 70:7468–7472.
- [40] Stewart KM, McLaughlin LW (2004) Four-arm oligonucleotide ni(ii)cyclam-centered complexes as precursors for the generation of supramolecular periodic assemblies. *JACS* 126:2050–2057.
- [41] Kristen M. Stewart, Javier Rojo LWM (2004) Ru(ii) tris(bipyridyl) complexes with six oligonucleotide arms as precursors for the generation of supramolecular assemblies. *Angewandte Chemie International Edition* 43:5808–5811.
- [42] Zanchet D, Micheel CM, Parak WJ, Gerion D, Alivisatos AP (2000) Electrophoretic isolation of discrete au nanocrystal/dna conjugates. *Nano Letters* 1:32–35.

- [43] Claridge SA, Liang HW, Basu SR, Fréchet JMJ, Alivisatos AP (2008) Isolation of discrete nanoparticledna conjugates for plasmonic applications. *Nano Letters* 8:1202–1206.
- [44] Bianchi E, Tartaglia P, Zaccarelli E, Sciortino F (2008) Theoretical and numerical study of the phase diagram of patchy colloids: ordered and disordered patch arrangements. *J Chem Phys* 128:144504.
- [45] Poole PH, Grande T, Angell CA, McMillan PF (1997) Polymorphic phase transitions in liquids and glasses. *Science* 17:322–323.
- [46] Likos CN, et al. (1998) Star polymers viewed as ultrasoft colloidal particles. *Phys. Rev. Lett.* 80:4450–4453.
- [47] Katayama Y, et al. (2000) A first-order liquid-liquid phase transition in phosphorus. *Nature* 403:170–173.
- [48] Poole PH, Sciortino F, Essmann U, Stanley HE (1992) Phase behaviour of metastable water. *Nature* 360:324–328.
- [49] Mishima O, Stanley HE (1998) Decompression-induced melting of ice iv and the liquid-liquid transition in water. *Nature* 392:164–168.
- [50] Scala A, Starr F, La Nave E, Stanley H, Sciortino F (2000) *Phys. Rev. E* 62:8016.
- [51] Debenedetti PG (2003) Supercooled and glassy water. *Journal of Physics: Condensed Matter* 15:R1669–R1726.
- [52] Brovchenko I, Geiger A, Oleinikova A (2003) Multiple liquid–liquid transitions in supercooled water. *The Journal of Chemical Physics* 118:9473–9476.
- [53] Poole P, Saika-Voivod I, Sciortino F (2005) Density minimum and liquid-liquid phase transition. *J. Phys.: Condens. Matter* 17:L431.
- [54] Glosli J, Ree F (1999) *Phys. Rev. Lett.* 82:4659.

- [55] Saika-Voivod I, Sciortino F, Poole P (2000) Computer simulations of liquid silica: equation of state and liquid-liquid phase transition. *Phys. Rev. E* 63:011202.
- [56] Saika-Voivod I, Sciortino F, Grande T, Poole PH (2004) Phase diagram of silica from computer simulation. *Phys. Rev. E* 70:061507.
- [57] Sastry S, Angell CA (2003) Liquid–liquid phase transition in supercooled silicon. *Nature Materials* 2:739–743.
- [58] Hsu CW, Starr FW (2009) Interpenetration as a mechanism for liquid-liquid phase transitions. *Phys. Rev. E* 79:041502.
- [59] Nykypanchuk D, Maye MM, van der Lelie D, Gang O (2007) Dna-based approach for interparticle interaction control. *Langmuir* 23:6305.
- [60] Maye MM, Nykypanchuk D, van der Lelie D, Gang O (2006) A simple method for kinetic control of dna-induced nanoparticle assembly. *Journal of the American Chemical Society* 128:14020–14021.
- [61] Maye MM, Nykypanchuk D, van der Lelie D, Gang O (2007) Dna-regulated micro- and nanoparticle assembly. *Small* 3:1678–1682.
- [62] Park SJ, Lazarides AA, Mirkin CA, Letsinger RL (2001) Directed assembly of periodic materials from protein and oligonucleotide-modified nanoparticle building blocks. *Ang. Chem.* 40:2909 – 2912.
- [63] Hobbie EK (1998) Metastability and depletion-driven aggregation. *Phys. Rev. Lett.* 81:3996–3999.
- [64] Liu H, Kumar SK, Douglas JF (2009) Self-assembly-induced protein crystallization. *Phys. Rev. Lett.* 103:018101.
- [65] Filobel LF, Galkin O, Vekilov PG (2005) Spinodal for the solution-to-crystal phase transformation. *J Chem Phys* 123:014904.

- [66] Galkin O, Vekilov PG (2000) Are nucleation kinetics of protein crystals similar to those of liquid droplets? *Journal of the American Chemical Society* 122:156–163.
- [67] Galkin O, Vekilov PG (2000) Control of protein crystal nucleation around the metastable liquid–liquid phase boundary. *PNAS* 97:6277.
- [68] Garetz BA, Matic J, Myerson AS (2002) Polarization switching of crystal structure in the nonphotochemical light-induced nucleation of supersaturated aqueous glycine solutions. *Phys. Rev. Lett.* 89:175501.
- [69] Bonnett P, Carpenter KJ, Dawson S, Davey. RJ (2003) Solution crystallisation via a submerged liquid-liquid phase boundary:oiling out. *Chemical Communications* pp 698–699.
- [70] Qian RY, Botsaris GD (2004) The effect of seed preparation on the chirality of the secondary nuclei. *Chem. Eng. Sci.* 59:2841–2852.
- [71] Lu PJ, et al. (2008) Gelation of particles with short-range attraction. *Nature* 453:499–503.
- [72] Pan W, Kolomeisky AB, Vekilov PG (2005) Nucleation of ordered solid phases of proteins via a disordered high-density state: Phenomenological approach. *J Chem Phys* 122.
- [73] Vekilov PG (2005) Two-step mechanism for the nucleation of crystals from solution. *Journal of Crystal Growth* 275:65–76.
- [74] Galkin O, Vekilov PG (1999) Direct determination of the nucleation rates of protein crystals. *The Journal of Physical Chemistry B* 103:10965–10971.
- [75] Dai W, Hsu CW, Sciortino F, Starr FW (2009) Valency dependence of polymorphism and polyamorphism in dna-functionalized nanoparticles. *Langmuir*.
- [76] Jr. ADM, Wiórkiewicz-Kuczera J, Karplus M (1995) An all-atom empirical energy function for the simulation of nucleic acids. *J. Am. Chem. Soc.* 117:11946–11975.

- [77] Konerding DE, T. E. Cheatham I, Kollman PA, James. TL (1999) Restrained molecular dynamics of solvated duplex dna using the particle mesh ewald method. *J. Biomol. NMR.* 13:119–131.
- [78] Young M, Ravishanker G, Beveridge D (1997) A 5-nanosecond molecular dynamics trajectory for b-dna: Analysis of structure, motions and solvation. *Biophys. J.* 73:2313–2336.
- [79] Jendrejack RM, de Pablo JJ, Graham MD (2002) Stochastic simulations of dna in flow: Dynamics and the effects of hydrodynamic interactions. *J. Chem. Phys.* 116:7752.
- [80] Ouldridge TE, Johnston IG, Louis AA, Doye JPK (2009) The self-assembly of dna holliday junctions studied with a minimal model. *J Chem Phys* 130:065101.
- [81] Largo J, Tartaglia P, Sciortino F (2007) Effective nonadditive pair potential for lock-and-key interacting particles: The role of the limited valence. *Phys. Rev. Lett. E* 76:11402.
- [82] Van Workum K, Douglas JF (2006) Symmetry, equivalence, and molecular self-assembly. *Phys. Rev. E* 73:031502.
- [83] Bianchi E, Largo J, Tartaglia P, Zaccarelli E, Sciortino F (2006) Phase diagram of patchy colloids: Towards empty liquids. *Phys. Rev. Lett.* 97:168301.
- [84] Wilding N (2001) Computer simulation of fluid phase transitions. *American Journal of Physics* 69:1147–1155.
- [85] Soto CM, Srinivasan A, Ratna BR (2002) Controlled assembly of mesoscale structures using dna as molecular bridges. *Journal of the American Chemical Society* 124:8508–8509.
- [86] Milam VT, Hiddessen AL, Crocker JC, Graves DJ, Hammer DA (2003) Dna-driven assembly of bidisperse, micron-sized colloids. *Langmuir* 19:10317–10323.

- [87] Sastry S, Nave EL, Sciortino F (2006) Maximum valency lattice gas models. *J. Stat. Mech.* p 12010.
- [88] Zaccarelli E, et al. (2005) Model for reversible colloidal gelation. *Phys. Rev. Lett.* 94:218301.
- [89] De Michele C, Gabrielli S, Tartaglia P, Sciortino F (2006) Dynamics in the presence of attractive patchy interactions. *The Journal of Physical Chemistry B* 110:8064–8079.
- [90] Frenkel D (2006) Colloidal crystals: Plenty of room at the top. *Nat. Mater.* 5:85–86.
- [91] Noya EG, Vega C, Doye JPK, Louis AA (2007) Phase diagram of model anisotropic particles with octahedral symmetry. *J Chem Phys* 127:054501.
- [92] Lindemann FA (1910) *Z. Phys.* 11:609.
- [93] Kittel C (2005) *Introduction to Solid State Physics* (Wiley Publishers, Hoboken, NJ).
- [94] ten Wolde PR, Ruiz-Montero MJ, Frenkel D (1996) Numerical calculation of the rate of crystal nucleation in a lennard-jones system at moderate undercooling. *J. Chem. Phys.* 104.
- [95] Fletcher NH (1970) *The Chemical Physics of Ice* (Cambridge University Press).
- [96] Rogers PH, et al. (2005) Selective, controllable, and reversible aggregation of polystyrene latex microspheres via dna hybridization. *Langmuir* 21:5562–5569.
- [97] Yanson IK, Teplitsky AB, Sukhodub LF (1979) Experimental studies of molecular interactions between nitrogen bases of nucleic acids. *Biopolymers* 18:1149 – 1170.
- [98] Osakada Y, Kawai K, Fujitsuka M, Majima T (2006) Charge transfer through dna nanoscaled assembly programmable with dna building blocks. *Proc. Nat. Acad. Sci. USA* 103:18072–18076.

- [99] Henderson PT, Jones D, Hampikian G, Kan Y, Schuster GB (1999) Long-distance charge transport in duplex dna: The phonon-assisted polaron-like hopping mechanism. *Proc. Nat. Acad. Sci. USA* 96:8353–8358.
- [100] Kelley SO, Barton JK (1999) Electron transfer between bases in double helical dna. *Science* 293:375–381.
- [101] Fink HW, Schönenberger C (1999) Electrical conduction through dna molecules. *Nature* 398:407–410.
- [102] Chernov AA (2003) Protein crystals and their growth. *Journal of Structural Biology* 142:3–21.